



ORIGINAL ARTICLE

Nuclear targeted multimodal 3D-bimetallic Au@Pd nanodendrites promote doxorubicin efficiency in breast cancer therapy



Adewale O. Oladipo^{a,*}, Jeremiah O. Unuofin^b, Solange I.I. Iku^b,
Thabo T.I. Nkambule^a, Bhekis B. Mamba^a, Titus A.M. Msagati^{a,*}

^a Institute for Nanotechnology and Water Sustainability (iNanoWS), College of Science, Engineering and Technology, University of South Africa, Science Park Florida, Johannesburg 1710, South Africa

^b Department of Life Sciences, College of Agriculture and Environmental Sciences, University of South Africa, Science Park Florida, Johannesburg 1710, South Africa

Received 20 April 2021; accepted 14 July 2021

Available online 19 July 2021

KEYWORDS

Bimetallic nanodendrites;
Doxorubicin;
Protamine sulfate;
Targeted delivery;
Hyperspectral imaging;
3D-CytoViva fluorescence
imaging

Abstract The therapeutic efficiency of doxorubicin (DOX) is dependent on its sufficient accumulation within the nucleus of cancer cells. Taking advantage of the fascinating properties (e.g., multiple dense arrays of hyperbranches and high surface area) of bimetallic nanodendrites as well as the arginine-rich components of protamine sulfate (PS), we herein present a new type of PS-modified Au@PdNDS-based hydrophobic drug carrier in which DOX can effectively bind to the surface of the PS.Au@PdNDS nanocarrier via non-covalent attachment. Chemical characterization of the synthesized PS.Au@PdNDS.DOX showed the successful loading of DOX onto the surface of PS.Au@PdNDS. Darkfield and Hyperspectral imaging analysis of the PS.Au@PdNDS.DOX demonstrated the time-dependent uptake and prolonged accumulation capability for releasing its DOX cargo inside the nucleus. Specifically, data from the 3D-CytoViva fluorescence imaging did not only track the nanocarrier's distribution but also confirmed its predominant accumulation in the nuclear compartment through clathrin-mediated endocytosis. Cytotoxicity assay showed that the PS.Au@PdNDS.DOX significantly inhibited cancer cell proliferation with maximum DOX release under acidic conditions (pH 4.5 and 5.5) than at normal physiological pH of 7.4. Moreover, the resultant PS.Au@PdNDS-based DOX nanocarrier efficiently improved the induction of apop-

* Corresponding authors at: Institute for Nanotechnology and Water Sustainability (iNanoWS), College of Science, Engineering and Technology, University of South Africa, Science Park Campus, Florida, Johannesburg 1710, South Africa.

E-mail addresses: walexxy20002001@gmail.com (A.O. Oladipo), msagatam@unisa.ac.za (T.A.M. Msagati).

Peer review under responsibility of King Saud University.



Production and hosting by Elsevier

tosis in MCF-7 cells compared to free DOX and passive targeted platform. In addition, loss of membrane integrity, mitochondria-apoptotic pathway, and internucleosomal DNA contents from cell cycle progression assay provided insights on the mechanism of cell death. Overall, the PS-Au@PdNDs-DOX nanocarrier may be employed for improved subcellular delivery of DOX as well as multimodal visualization in cancer therapy.

© 2021 The Authors. Published by Elsevier B.V. on behalf of King Saud University. This is an open access article under the CC BY-NC-ND license (<http://creativecommons.org/licenses/by-nc-nd/4.0/>).

1. Introduction

For many decades, doxorubicin; an anticancer/antineoplastic drug remains at the forefront of chemotherapy in the fight against various types of cancer (Rayner and Cutts, 2014). Its mechanisms of action include the induction of apoptosis (Pilco-Ferreto and Calaf, 2016), DNA damage (Halim et al., 2018), topoisomerase II poisoning (Marinello et al., 2018), and generation of free radicals (Sinha, 2020). Despite its fascinating clinical efficacy against many kinds of cancer, the use of anticancer drugs has been plagued with a short half-life, rapid metabolism, and inability to discriminate between cancerous cells and normal cells (Carvalho et al., 2009; Maney and Singh, 2019). Also, the poor absorption of anticancer drugs within the interstitials after administration often leads to their accumulation in the reticuloendothelial (RES) systems, hence resulting in poor treatment outcomes and in some cases cancer relapse (Oladipo et al., 2017). Moreover, there has been a myriad of challenges relating to its side effects which could be life-threatening in many cases and can affect a patient's quality of life after chemotherapy (Maney and Singh, 2017). Hence, the development of an alternative and efficient platform for achieving improved therapy would be highly beneficial.

It has been proposed that enhanced DOX cytotoxicity can be achieved through its discharge directly into the nucleus where it intercalates with the DNA double helix and subsequently prevents DNA replication (Jang et al., 2013; Wu et al., 2019; Yang et al., 2016). Generally, DOX-nanocarriers are mostly internalized and accumulate in the cytoplasm but rarely get to the nucleus. Reports have highlighted that only about 0.4% of DOX enter the nucleus after cellular uptake (Li et al., 2019; Mizutani et al., 2005). This is because the nuclear transport of nanocarriers is complex due to the pore diameter of the nuclear membrane. The spontaneous uptake of nanocarriers by the nuclear compartment should allow for more efficient diffusion of DOX and address the challenge of DOX inefficiency.

Several nuclear-targeted drug nanocarriers including smart polymers (Zhong et al., 2015) and cell-penetrating peptides (CPPs) (Yu et al., 2018) have been reported. Smart nanocarriers with stimuli-responsive properties are particularly interesting in targeted therapy and are considered promising platforms for improved chemotherapy. The encapsulation of DOX and purpurin 18 by cyclodextrin-based polymeric micellar system with reactive oxygen species (ROS) responsive properties was reported to improve drug treatment efficiency from a combined photodynamic-chemotherapy redox strategy (Jia et al., 2021). Also, DOX-loaded oxidized cellulose nanoparticles with potential pH-triggered release showed enhanced site-specific drug delivery under the acidic tumor microenvironment (Kumari et al., 2018). In contrast, amino-rich cationic poly-

mers like protamine sulfate (PS) present an interesting natural, low-molecular-weight polymer with excellent biocompatibility and biodegradability (Cao et al., 2013). It is a highly cationic peptide comprising an arginine-based amino acid with strong alkalinity (Xie et al., 2018), and rich in nuclear localization signal (NLS) (Puras et al., 2015). Its arginine-rich structure can directly bind onto nanoparticles which influences the cell signaling pathway for molecules to cross the plasma membrane into cells. Moreover, PS ligand on the surface of nanocarriers can provide a high affinity for nucleus-specific trafficking, thereby providing a fantastic opportunity for enhanced drug delivery and improving drug targeting potentials.

Advancements in nanomedicine have led to the development of many delivery vehicles for DOX which have largely been able to mitigate these outlined issues of anticancer administration. These drug delivery vehicles include metal nanoparticles (Du et al., 2018), carbon nanotubes (Ünlü et al., 2018), polymeric nanoparticles (Nair, 2019), micelles (Wang et al., 2020), etc. have been extensively deployed as drug nanocarriers. Among these nanocarrier-systems, three-dimensional (3D) dendritic-shaped bimetallic nanoparticles are gaining interest since they possess excess morphology, three-dimensional architecture (Oladipo et al., 2020b), synergistic capabilities (X. Liu et al., 2017), and can provide a high surface area required to improve drug loading (Calamak and Ulubayram, 2019). For example, our group introduced Au@Pd bimetallic nanodendrites with three-dimensional morphological structures, which were capable of improving DOX-loading by ~90% and showed stimuli-responsive properties (Oladipo et al., 2020). Similarly, DOX-loaded cRGD peptide modified Au@Pt nanodendrites combined chemophotothermal treatment was reported by Yang group (Yang et al., 2018). The cRGD-Au@PtNPs/DOX enhanced the delivery of DOX and simultaneously demonstrated the potential for scavenging reactive oxygen species (ROS) resulting from DOX-induced oxidation. While previous studies on dendritic-shaped nanoparticles are useful for improving DOX efficiency, several issues relating to real-time tracking, nuclear transport, and subcellular retention still require further investigation. Moreover, the highly active surfaces of palladium (Phan et al., 2020) in a synergistic combination with the tunable optical properties of gold (Qiu et al., 2016) should provide a platform for improved conjugation of ligands and drug molecules with enhanced targeted therapeutic functionalities. With good biocompatibility, higher near-infrared (NIR) absorption, and efficient multimodal imaging capabilities (Phan et al., 2020), palladium remains an emerging metal of choice in the fabrication of bimetallic nanodendrites for biomedical applications.

Motivated by this discovery, we fabricated a bimetallic nanocarrier (Au@PdNDs) with multiple dense arrays of

branches which were modified with protamine sulfate for improved subcellular transport. DOX was subsequently conjugated to the PS-modified Au@PdNDS and the resultant PS-Au@PdNDS.DOX nanocarrier was applied to deliver DOX into the nucleus. The subcellular uptake, accumulation, and distribution of the PS.Au@PdNDS.DOX were studied using darkfield, hyperspectral imaging, and 3D-CytoViva fluorescence microscopy. Furthermore, superior DOX therapeutic efficacy induced by the PS-nanocarrier in breast carcinoma MCF-7 cells was observed when compared with DOX alone and passive-targeted PEG-modified DOX-nanocarrier.

2. Materials and methods

2.1. Materials

Gold chloride (HAuCl₄, 99.9%), Sodium tetrachloropalladate (II) (99%), D-Glucose (99%), Poly (ethylene glycol) methyl ether thiol (mPEG-SH, M_w 2000), L-ascorbic acid (AA, 98%), octadecylamine (ODA 90%, technical grade), doxorubicin (DOX, 99%), Protamine sulfate (grade X salt from salmon), Dulbecco's modified (DMEM) cell culture medium, streptomycin-penicillin, fetal bovine serum (FBS), Trypsin-EDTA (0.25%), and Mitochondrial membrane potential assay kit (MAK 159) were purchased from Merck (Johannesburg, South Africa). CellTiter-Blue reagent and CytoTox-ONE Homogenous membrane integrity reagent were purchased from Promega (Madison, WI, USA). MUSE Annexin V & Dead Cell reagent and MUSE Cell Cycle Kit were purchased from Luminex Corp. (Austin, TX, USA). Ethanol, chloroform, and dimethylsulfoxide (DMSO) were purchased from ThermoFisher. All chemicals were used as received. Ultrapure water produced from a Milli-Q-purification system (resistivity, 18.2 MΩcm⁻¹) was used in all experiments.

2.2. Synthesis and characterization of PS.Au@PdNDS.DOX

Bimetallic gold-core palladium dendritic-shell nanoparticles (Au@PdNDS) were synthesized following the method earlier reported (Oladipo et al., 2020; Zhou et al., 2014). 2 mg mPEG-SH was added to a 2 mg/mL of Au@PdNDS dispersed chloroform under gentle sonication to make the nanodendrites water-soluble. After 12 h, the solution was centrifuged twice at 13,200 rpm for 40 min at 4 °C and the pellets redispersed in water. Thereafter, protamine modified Au@PdNDS was prepared by slowly mixing 2 mg/mL protamine sulfate salt dissolved in deionized water to 2 mL PEGylated Au@PdNDS solution under gentle sonication and incubated overnight with periodic shaking. The PS modified Au@PdNDS were ultracentrifuged twice and the pellets redispersed in 2 mL deionized water. Then, 2 mg DOX dissolved in 20 μL of deionized water was mixed with the PS-modified Au@PdNDS solution and stirred in the dark for 8 h. The resulting PS.Au@PdNDS.DOX conjugate was centrifuged to remove unbound drugs and the obtained pellets redispersed in water for further analysis.

2.3. Physicochemical properties of PS.Au@PdNDS.DOX

The morphological characterization of the PS.Au@PdNDS and its DOX conjugate were examined by transmission elec-

tron microscopy (TEM), high-resolution transmission electron microscopy (HRTEM), and selected area electron diffraction (SAED). TEM and HRTEM images were obtained from a JEOL JEM 2100 operated at an accelerating voltage of 200 KV. The functional groups on the surface of the nanoconjugate were analyzed using a PerkinElmer Frontier Fourier transform infrared (FTIR) spectroscopy fitted with a universal attenuated total reflectance (ATR) detector in the range of 500–4000 cm⁻¹. The hydrodynamic diameter and surface charge of the nanoconjugate were determined using a Nano ZS Zetasizer (Malvern, Worcestershire, UK). The size of the nanocarrier was observed over 8 days in an aqueous solution. Fluorescence spectra and UV–vis absorption were recorded on Fluorolog 3 (FL-1057, HORIBA, Japan) and PerkinElmer Lambda 650 UV–Vis spectrophotometer, respectively.

2.4. DOX loading and optimization

2.4.1. DOX loading efficiency

The percentage and rate of DOX loading onto the PS.Au@PdNDS were determined by ultracentrifugation. The PS.Au@PdNDS suspension (1 mg/mL) was incubated with DOX solution (1 mg/mL) and monitored at 4 °C for 24 h. At predetermined intervals, 20 μL aliquots were withdrawn from the solution mixture and measured for DOX contents. The concentration of DOX loaded onto the PS.Au@PdNDS and unloaded DOX were quantified after centrifugation at 13,200 rpm for 30 min at 4 °C (Eppendorf centrifuge 5415R). DOX contents were analyzed for fluorescence using ELISA, (Thermo Fisher Scientific Oy, Vantaa, Finland) at 488/582 nm excitation/emission wavelength. A standard calibration plot of free DOX (0–100 μg/mL) was obtained under similar conditions. The loading efficiency and loading content of the PS.Au@PdNDS was calculated using the equation below:

$$\text{Loading efficiency (\%)} = \frac{DOX_{used} - DOX_{free}}{DOX_{used}} \times 100 \quad (1)$$

$$\text{Loading content (\%)} = \frac{DOX_{used} - DOX_{free}}{\text{Weight of nanocarrier}} \times 100 \quad (2)$$

To optimize the PS.Au@PdNDS loading efficiency, DOX (1 mg/mL) was incubated with PS.Au@PdNDS suspension (1 mg/mL) in a (v/v) ratio and left overnight at 4 °C. The amount of DOX per PS.Au@PdNDS were determined by measuring the fluorescence intensity of unloaded DOX present in the supernatant after centrifugation. A standard fluorescence intensity calibration plot of free DOX (0–100 μg/mL) was used to evaluate the DOX contents using ELISA, (Thermo Fisher Scientific Oy, Vantaa, Finland) with excitation wavelength at 482 nm and emission at 582 nm.

2.4.2. In vitro DOX release at different pH

The in vitro DOX release kinetics from PS.Au@PdNDS.DOX were investigated under physiological conditions (pH 4.5, 5.5, and 7.4) at 37 °C for 72 h using a shaking incubator. 5 mg of PS.Au@PdNDS.DOX was dispersed in a 5 mL PBS solution and placed in a temperature-controlled shaking incubator. A 50 μL aliquot of the solution was collected at intervals and replaced with an equal volume of fresh PBS. The amount of DOX content was analyzed using ELISA as described above.

2.5. Cell culture

MCF-7 (human breast adenocarcinoma) and human embryonic kidney (HEK 293) cells were obtained from the European Collection of Authenticated Cell Cultures (ECACC) through Merck, South Africa. The cells were cultured in Dulbecco's Modified Eagle's Media (DMEM) supplemented with 10% fetal bovine serum (FBS) and 1% L-glutamine-penicillin-streptomycin under 5% CO₂ incubation at 37 °C. At 80% confluence, the cells were detached with trypsin-EDTA. The cells were centrifuged and then resuspended in the growth medium for seeding.

2.5.1. Cytotoxicity assay

The CellTiter-Blue fluorescence assay was used to determine the cytotoxicity of the nanoconjugates. 2×10^4 cells/mL of MCF-7 and HEK 293 cells were seeded in a 96-wells plate and incubated at 50 µL/well for 24 h (37 °C, 5% CO₂). The cells were treated with 50 µL sample suspensions of DOX and its nanodendrite conjugates at different concentrations (5, 10, 25, 50 µg/mL) for 24 h incubation. Thereafter, a 20 µL of CellTiter-Blue reagent was added to each well and the plates were gently shaken before being incubated for 4 h. Fluorescence intensities associated with each well were measured using a microplate reader (ELISA, Thermo Fisher Scientific Oy, Vantaa, Finland) at 560 nm excitation and 590 nm emission wavelength. Fluorescence data were normalized to control cells and the percentage cell viability was calculated. All experiments were conducted in triplicate.

2.5.2. Cell uptake analysis

CytoViva imaging techniques were used for cell uptake, internalization, and distribution analysis. See [Supplementary information](#) for the detailed protocol.

2.5.3. Annexin V & Dead cell assay (Flow cytometry)

The induction of apoptosis by DOX, Au@PdNDs.PEG/DOX, and PS.Au@PdNDs.DOX on Human breast carcinoma (MCF-7 cells) was assessed using the GUAVA MUSE Cell Analyzer (Luminex Corp. TX, USA). MCF-7 cells were seeded in a 6-well plate at 1×10^5 cells for 24 h. The cells were treated with respective IC₅₀ values for DOX, Au@PdNDs.PEG/DOX, and PS.Au@PdNDs.DOX, and untreated cells were used as a negative control for 24 h and 48 h. After incubation, the cells were trypsinized and washed twice with 1 mL PBS before resuspension. Thereafter, the cells were resuspended in fresh 100 µL PBS under gentle vortexing in a 1.5 mL Eppendorf tube. A 100 µL of Annexin V & Dead Cell reagent was added to the cells and subsequently incubated for 20 min in the dark at room temperature. The cell apoptosis was analyzed using the MUSE Cell Analyzer equipped with a MUSE analysis software module system. All experiments were performed in triplicate and the results were grouped into live, early apoptosis, late apoptosis, and dead cells.

2.5.4. Cell cycle assay

MCF-7 cells were seeded in a 6-well plate at 2×10^5 cells/well for 24 h as described above. After treatment with DOX,

Au@PdNDs.PEG/DOX, and PS.Au@PdNDs.DOX at IC₅₀ values for 24 h, cells were transferred into a 1.5 mL Eppendorf tube and centrifuged at 1500 rpm for 5 min. Thereafter, the cells were washed with PBS before being fixed with 70% ice-cold ethanol at -20 °C for 4 h. The fixed cells were centrifuged, washed, and the pellets resuspended in an Eppendorf tube with 200 µL PBS. A 200 µL of MUSE Cell Cycle reagent (Millipore, MA, USA) was then added to the cells and the tubes containing the cell-reagent mixture were incubated for 30 min in the dark at room temperature. The cell cycle phases were analyzed using the GUAVA MUSE Cell Analyzer (Luminex Corp. TX, USA) equipped with an analyzer software module system. Cells were categorized into three groups: G0/G1, S, and G2/M phases.

2.5.5. Mitochondrial membrane potential assay

MCF-7 cells were treated with DOX, Au@PdNDs.PEG/DOX, and PS.Au@PdNDs.DOX at IC₅₀ values. After 24 h of incubation, 50 µL of cell media were carefully removed and 25 µL of Dye loading solution was added to each well. Following 30 min incubation, 25 µL of assay buffer B was added to the wells and the plate was incubated for 30 min. The fluorescence intensities were measured at 490/525 nm (green) and 540/590 nm (red) excitation/emission wavelengths. The mitochondrial membrane potential was determined from the ratio of red/green fluorescence intensities.

2.5.6. Necrosis assay

Necrotic cell death resulting from a compromise of cell membrane integrity was measured using a Lactate dehydrogenase (LDH) detection kit ([Hiebl et al., 2017](#)). MCF-7 cells treated with DOX, Au@PdNDs.PEG/DOX, and PS.Au@PdNDs.DOX at IC₅₀ values for 24 h were incubated with 100 µL of reconstituted CytoTox-ONE reagents. A 2 µL of lysis solution (9% Triton X-100) was used as a positive control to induce a maximum release of LDH from cells. The plates were incubated for 10 min and followed by the addition 50 µL of stop solution before fluorescence measurements for treated (test samples) and untreated cells (control) were obtained at 560/590 nm excitation/emission wavelengths on a microplate reader (ELISA, Thermo Fisher Scientific Oy, Vantaa, Finland). The average fluorescence values corrected against the medium background and the percentage of LDH released were calculated from the below equation:

$$LDH \text{ release } (\%) = \frac{\text{Experimental} - \text{Medium background}}{\text{Maximum LDH} - \text{Medium background}} \times 100 \quad (3)$$

2.6. Statistical analysis

All data are presented as mean \pm standard deviation (SD). The differences between groups were analyzed by a simple *t*-test followed by the Wilcoxon test for multiple comparisons. Statistical analyses were performed using GraphPad Prism 8.3 and significance denoted as **P* < 0.05, ***P* < 0.01 and ****P* < 0.001.

3. Results and discussion

3.1. Synthesis and characterization of PS-modified Au@PdNDs.DOX

Biocompatible and water-soluble PEGylated bimetallic gold-core, palladium nanodendrites (Au@PdNDs.PEG) were synthesized using the previously reported method (Oladipo et al., 2020). The synthesized Au@PdNDs.PEG were mixed with PS under gentle shaking at room temperature to obtain the PS.Au@PdNDs via electrostatic interactions (Ji et al., 2018; Xie et al., 2018), since PS and Au@PdNDs.PEG are of opposite charges (positive and negative charges, respectively). After repeated centrifugation to remove unbound PS from the PS-modified Au@PdNDs, the anticancer drug doxorubicin (DOX) was loaded onto the surface of the PS.Au@PdNDs to obtain a tumor-targeting PS.Au@PdNDs.DOX delivery system (Fig. 1). The purified PS-based

Au@PdNDs.DOX drug nanocarrier was used for characterization.

Fig. 2A shows the transmission electron microscopy (TEM) image of the resulting PS.Au@PdNDs. The PS.Au@PdNDs nanocarrier displayed the spherical gold-core (diameter, ~12 nm) surrounded by palladium dendritic shells with multiple dense arrays of branches. The high-resolution TEM (HRTEM) image shows the DOX evenly distributed on the surface of the PS.Au@PdNDs.DOX nanocarrier (Fig. 2B). Moreover, the crystalline nature of the PS.Au@PdNDs.DOX can be observed with bright spots in the selected area electron diffraction pattern (Fig. 2C). The formation of the PS.Au@PdNDs.DOX was also investigated by zeta-potential changes. The Au@PdNDs.PEG possessed an initial zeta potential value of -18.25 mV which changed to a positive charge ($+12.43$ mV) when the surface was modified with protamine sulfate (Fig. 2D). The reversal of charge was attributed to the polycationic nature of protamine. After DOX loading,

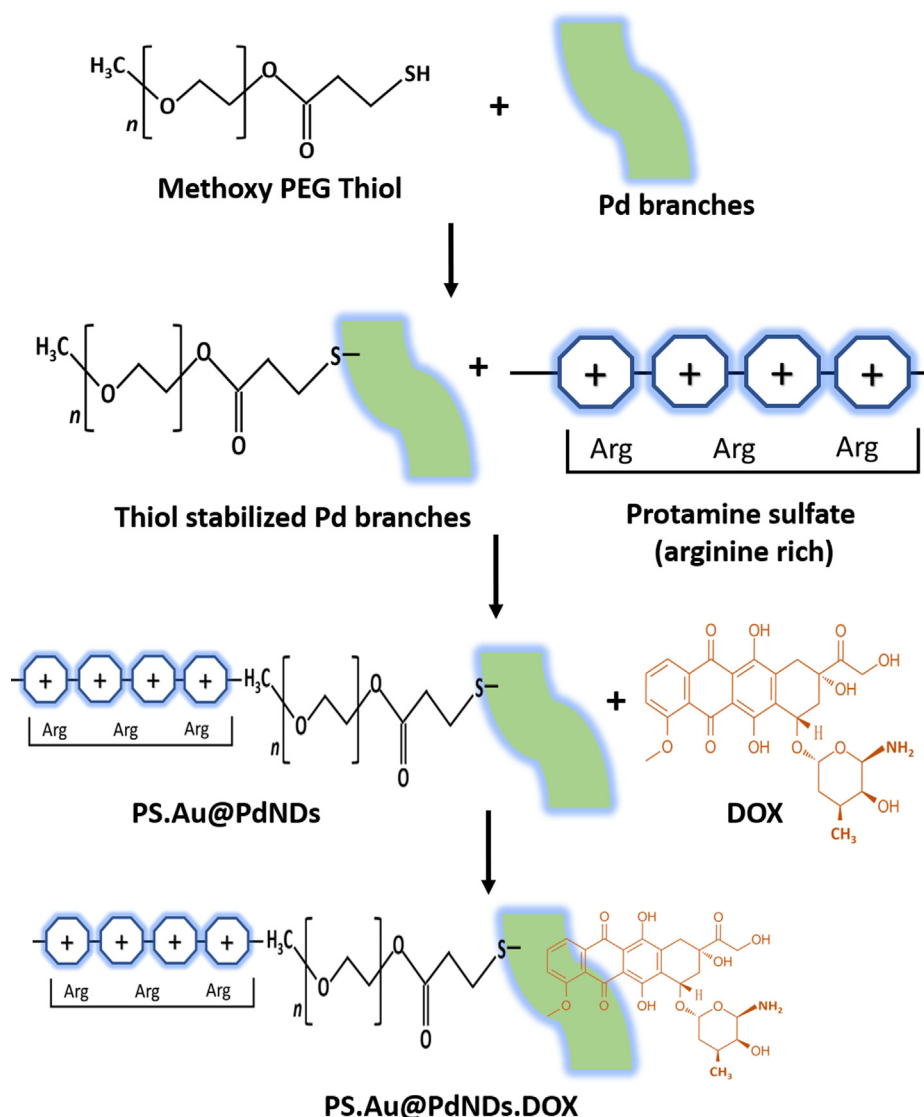


Fig. 1 Illustration showing the preparation of PS-modified Au@PdNDs and subsequent DOX conjugation.

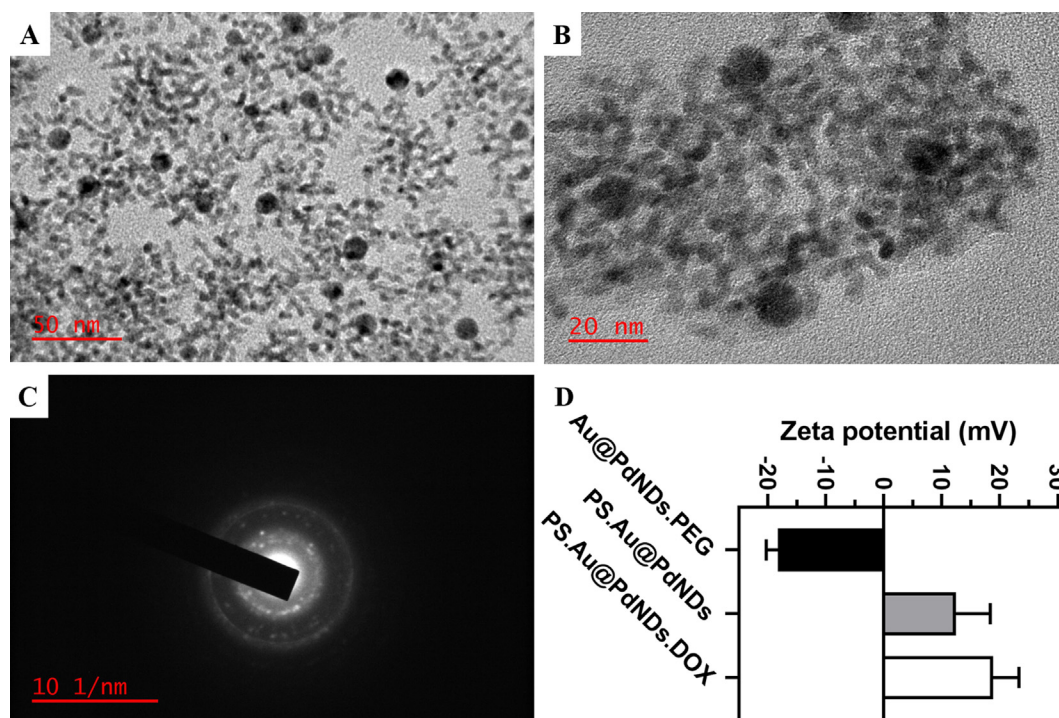


Fig. 2 Characterization of PS.Au@PdNDs. (A) TEM image, (B) HRTEM of PS.Au@PdNDs.DOX, (C) Selected-area electron diffraction (D) Zeta-potential changes accompanying the formation of PS.Au@PdNDs.DOX nanocarrier ($n = 3$).

the surface charge increased further to +18.9 mV due to the positive charge of DOX molecules which caused the charge to increase.

The presence of DOX on the surface of PS.Au@PdNDs. DOX was also established by characterizing the solution of the DOX-loaded nanocarrier using fluorescence and UV-Vis spectroscopy. At an excitation wavelength of 488 nm, free DOX showed maximum emission at 598 nm and 637 nm while the PS.Au@PdNDs.DOX showed DOX fluorescence predominantly quenched due to the complexation of DOX with the PS.Au@PdNDs nanocarrier (Fig. 3A). The weak emission peaks noticed at 552 nm and 591 nm in the PS.Au@PdNDs. DOX solution (with the same DOX concentration) which blue-shifted could be attributed to the non-covalent attachment of DOX molecules with the surfaces of the PS. Au@PdNDs or high concentration of DOX on the nanocarrier surfaces resulting from self-quenching of DOX (Benyettou et al., 2017). In Fig. 3B, UV absorption spectra of DOX exhibited a distinctive peak at 492 nm while the PS. Au@PdNDs displayed a broad absorption spectrum. Upon the conjugation of DOX onto the PS.Au@PdNDs, an additional shoulder peak characteristic of DOX which red-shifted to 533 nm was located on the formed PS.Au@PdNDs.DOX nanocarrier. These results indicated that DOX was successfully conjugated to the surface of the nanocarrier (Oladipo et al., 2021).

Similarly, the structural changes that characterize the formation of the PS.Au@PdNDs.DOX were studied by FTIR analysis. In Fig. 3C, we observe a disappearance of the NH_2 stretching peak (3255 cm^{-1}) while the symmetric and asymmetric CH_2 peaks ($2911\text{--}2847 \text{ cm}^{-1}$) remain in the

octadecylamine (ODA)-capped Au@PdNDs. We attributed this to the complexation between the Pd-dendritic shells and —N—H stretching of the ODA. The peaks at 1059 cm^{-1} to 900 cm^{-1} completely disappeared from the spectrum of the Au@PdNDs.ODA, thus indicating an interaction between Au@PdNDs and ODA. After ligand exchange with mPEG-SH, the spectrum of Au@PdNDs.PEG displayed 2864 cm^{-1} and 1094 cm^{-1} peaks corresponding to —CH_2 and —C—O vibrations which confirmed covalent bound PEG coating on the surface of the water-soluble Au@PdNDs.PEG. For the PS-modified Au@PdNDs, the peak at 3274 cm^{-1} was attributed to the NH_3^+ of the amino acid salt (Fig. 3D). Several other distinctive peaks such as stretching amide I (1636 cm^{-1}), amide II (1530 cm^{-1}), S=O organic sulfate salt (1456 cm^{-1}) and stretching arginine (1068 cm^{-1}) of protamine sulfate were also present in the PS.Au@PdNDs. Upon DOX-loading onto the PS.Au@PdNDs, distinctive peaks at 2983 cm^{-1} (symmetric CH_2), 1648 cm^{-1} (C=O bond), 1412 cm^{-1} (C—C in bond), and 883 cm^{-1} (primary amine NH_2) of DOX were visible. These additional peaks generated in the spectrum of PS. Au@PdNDs.DOX are associated with the DOX fingerprint region suggested the successful conjugation of the PS. Au@PdNDs with DOX molecules.

The stability of the PS.Au@PdNDs.DOX incubated in PBS (pH 7.4) at 37°C was investigated using the Dynamic light scattering technique (DLS). The hydrodynamic diameter of PS.Au@PdNDs.DOX in Fig. S1A indicated that the nanocarrier was stable for 8 days with sizes $< 100 \text{ nm}$. In addition, the zeta potential was measured within the same period with the PS.Au@PdNDs.DOX nanocarrier showing a negligible increase in values (Fig. S1B). Both particle size and zeta poten-

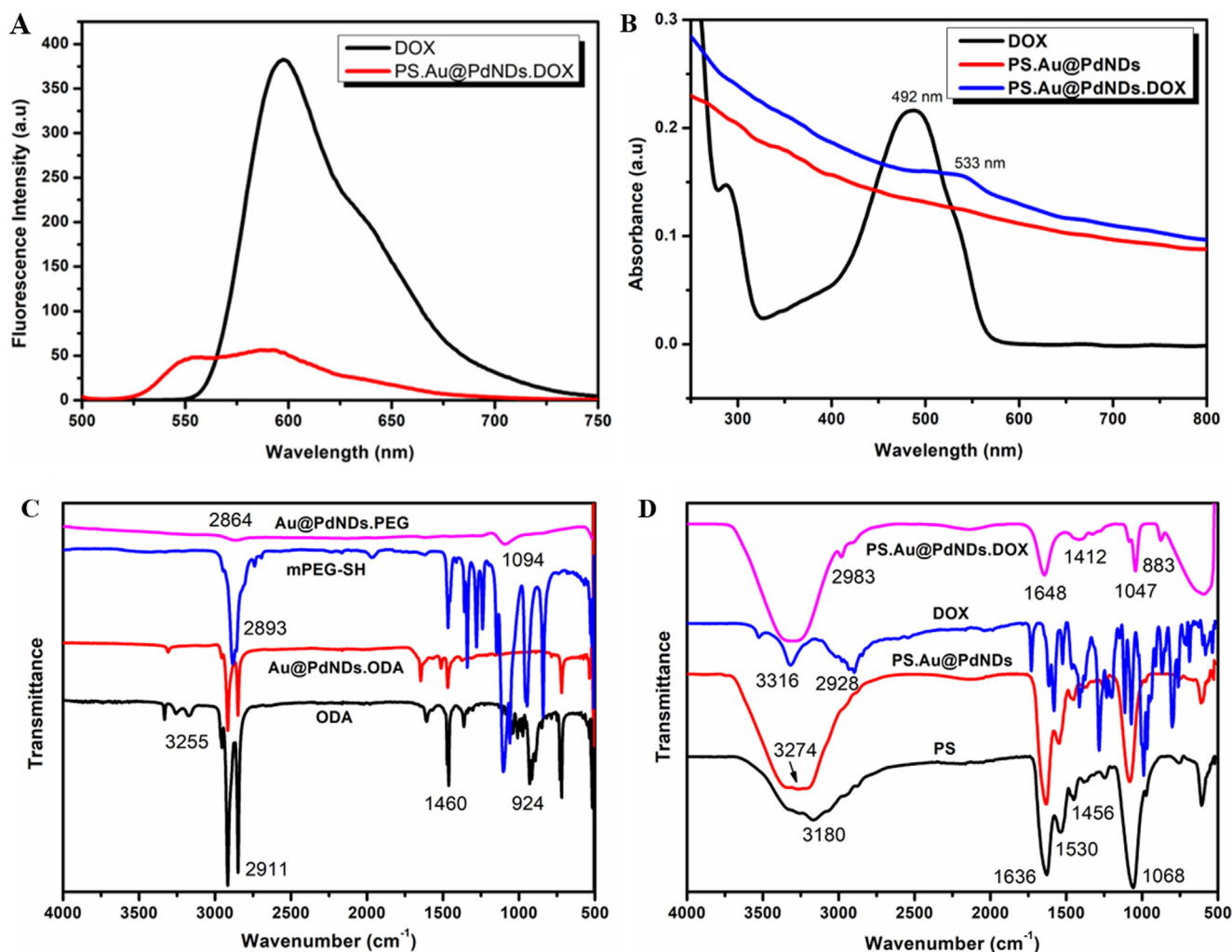


Fig. 3 Fluorescence spectra of (A) free DOX and DOX-conjugated PS.Au@PdNDs and (B) UV-Vis absorption spectra of free DOX, PS.Au@PdNDs, and PS.Au@PdNDs.DOX nanocarrier, FTIR spectra of (C) ODA, Au@PdNDs.ODA, mPEG-SH, and Au@PdNDs.PEG (D) PS, PS.Au@PdNDs, DOX, and PS.Au@PdNDs.DOX.

tial are important properties because they provide invaluable information that influences the stability, cell uptake, and the consequent biological performance of nanocarriers.

3.2. DOX loading onto PS.Au@PdNDs and its release evaluation

The dynamics of DOX loading onto PS-modified Au@PdNDs were studied using fluorescence measurements based on the quenching of DOX fluorescence by nanocarrier (Fig. S2). Several loading experiments were performed to investigate the maximum loading capacity of the PS.Au@PdNDs nanocarrier. After optimization, a loading efficiency (LE) of ~79.41% and loading content (LC) of ~50.21% was achieved at 4:1 PS.Au@PdNDs:DOX ratio (Table S1). Using this optimized ratio, the loading kinetic pattern of DOX onto the PS.Au@PdNDs nanocarrier was studied. An LC of ~75% was achieved at 1 h incubation and subsequently increased with time (Fig. 4 A). The rapid loading of DOX could be attributed to the increased binding sites on the nanodendrites which were

mediated by electrostatic forces. At 24 h, an LC of ~80% was attained with no further increase in LC afterward, indicating that equilibrium was reached. The pH-responsive properties of the optimized PS.Au@PdNDs.DOX nanocarrier were studied at pH 4.5, 5.5, and 7.4 to simulate the intracellular and extracellular conditions. Following endocytosis, the endosomal vesicles formed around nanocarriers undergo rapid acidification due to ATPase-mediated proton invasion. This results in the pH levels of endosomes to rapidly drop to < 6.0, thereby mediating endosomal rupture and subsequent nanocarrier release. Fig. 4B shows the DOX release profiles from PS.Au@PdNDs.DOX nanocarrier. At acidic pH, the PS.Au@PdNDs.DOX displayed an enhanced drug release rate. Specifically, as much as 80% (pH 4.5) and 49% (pH 5.5) of DOX were release at 6 h and continued to increase up to 36 h. When DOX-loaded nanocarriers enter the cell, structural deformation is initiated by the acidic pH of the tumor environment (pH 6.5) particularly at the endosomal and lysosomal pH of 4.5–5.5. These different hydrolysis rates induced by the acidic tumor microenvironment lead to an inevitable rapid release of DOX from the nanocarrier system (Benyettou

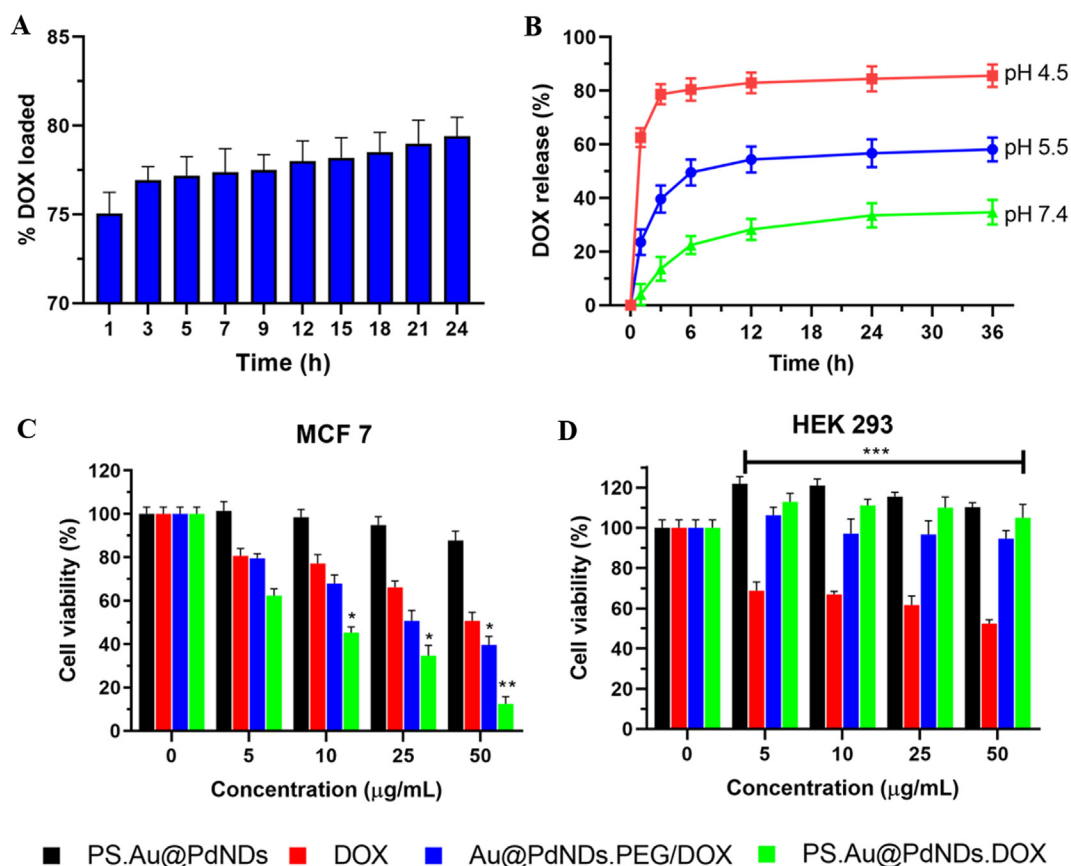


Fig. 4 In vitro DOX loading kinetics showing the percentage of (A) DOX loaded onto PS.Au@PdNDs; DOX:PS.Au@PdNDs ratio of 1:4 (B) DOX release profile from PBS at pH 4.5, 5.5, and 7.4, cytotoxicity of PS.Au@PdNDs, DOX, Au@PdNDs.PEG/DOX, and PS.Au@PdNDs.DOX on (C) MCF-7 and (D) HEK 293 cells for 24 h. Data are presented as mean \pm standard deviation ($n = 3$). Statistical differences between groups are * $P < 0.05$, ** $P < 0.01$ and *** $P < 0.001$.

et al., 2017; Cavalcante et al., 2021). Under normal conditions (pH 7.4), only about 33% of DOX was released after 24 h, which should reduce systemic toxicity commonly associated with DOX under physiological pH (Oladipo et al., 2020a). A higher amount of DOX released under acidic conditions showed the selective release capacity of PS.Au@PdNDs. DOX which are beneficial for promoting pH-responsive drug nanocarrier's efficiency in cancer therapy.

3.3. Cell cytotoxicity studies using PS.Au@PdNDs.DOX

The inhibition of cell proliferation by the different DOX formulations on MCF-7 and HEK 293 cells was investigated using a fluorescence-based assay. In this assay, free DOX and passive targeted Au@PdNDs.PEG/DOX were set as positive controls. The viability of MCF-7 cells treated with various formulations of DOX showed a concentration-dependent decrease as shown in Fig. 4C. For instance, free DOX, Au@PdNDs.PEG/DOX, and PS.Au@PdNDs.DOX at a concentration of 10 $\mu\text{g/mL}$ suppressed MCF-7 cells' growth with 77.2%, 67.9%, and 45.3% viability, respectively. More importantly, the PS.Au@PdNDs.DOX exhibited significantly greater cytotoxicity (34.7% at 25 $\mu\text{g/mL}$ and 12.5% at 50 $\mu\text{g/mL}$) after treatment with the equivalent DOX dosage compared with free DOX and Au@PdNDs.PEG/DOX. The

calculated IC_{50} values for PS.Au@PdNDs.DOX further showed that a lower dosage, 3.05 $\mu\text{g/mL}$ is required to inhibit the proliferation of MCF-7 cells (Table 1). In contrast, the PS-modified Au@PdNDs showed no obvious toxicity even at a high concentration of 50 $\mu\text{g/mL}$ (~90% viable cells), therefore suggesting that the PS.Au@PdNDs are non-cytotoxic and biocompatible. A similar dose-response effect was noticed from the various DOX formulation treatments against HEK 293, a representative non-cancerous somatic cell line. Specifically, DOX alone showed reduced cell viability (68.7–52.3%) with increasing concentrations (Fig. 4D). However, both PS.Au@PdNDs and PS.Au@PdNDs.DOX treatment did not result in any cytotoxicity with viable cells above 110.2% and 105.1% respectively, at 50 $\mu\text{g/mL}$. Although both cells were more sensitive to DOX treatment, these results suggest the preferential uptake of PS.Au@PdNDs.DOX by MCF-7 cells than HEK 293 as treatment did not affect non-cancerous cells. Also, the significantly enhanced antitumor chemotherapeutic response of PS.Au@PdNDs.DOX over free DOX noticed in MCF-7 cells may be attributed to the slow and sustained release of DOX from PS.Au@PdNDs.DOX nanocarrier (Yuan et al., 2017). Since DOX uptake occurs predominantly via a passive diffusion mechanism (Suarasan et al., 2016), the rapid uptake and intracellular transport of the PS.Au@PdNDs.DOX nanocarriers can efficiently mediate the

Table 1 Calculated IC₅₀ values for Au@PdNDs.PEG, DOX, Au@PdNDs.PEG/DOX, and PS.Au@PdNDs.DOX in MCF-7 cells from cytotoxicity assays.

Cell line	PS.Au@PdNDs	DOX	IC ₅₀ values (μg/mL)	
			Au@PdNDs.PEG/DOX	PS.Au@PdNDs.DOX
MCF-7	21.92	9.58	8.56	3.05

time-dependent release of DOX closer to the nucleus, thereby leading to increased concentration of DOX. Hence, the cytotoxicity results strongly suggest that DOX delivery using active-targeted nanocarrier PS.Au@PdNDs could efficiently improve the anticancer activity of DOX. Moreover, the investigation of the mechanism of action regarding the selectivity of PS.Au@PdNDs.DOX nanocarrier should be relevant in future work.

3.4. Cell uptake studies using PS.Au@PdNDs.DOX

3.4.1. Enhanced darkfield microscopy

The ability of nanocarriers to pass through tumor vasculature and be localized at the disease target site is the hallmark of successful therapy. Therefore, to visualize and track the accumulation of nanocarrier systems in cells, we utilize darkfield microscopy, hyperspectral imaging, and spectral angle mapping. Interestingly, the light scattering properties of Au@PdNDs present a fascinating tool for visual monitoring of the PS.Au@PdNDs.DOX nanocarrier system. Fig. 5 shows

the darkfield microscopy images of MCF-7 cells treated with PS.Au@PdNDs.DOX at different exposure times. The slight glow noticed in the untreated cells emanated from the intrinsic visible light scattering inherent in cellular organs (Fig. 5A) (Suarasan et al., 2016). After 2 h of exposure, the cells show narrow scattering coming from the DOX-loaded PS.Au@PdNDs (Fig. 5B). Most of the observed light scattering at this time point was concentrated around the cell membrane. At 6 h, a strong optical scattering was observed which became most intense at 24 h with the majority of the bright spots significantly located in the interior of the cells and possibly within the nucleus (Fig. 5C-D). This observation demonstrated that the PS.Au@PdNDs.DOX were accumulated within the cells in a time-dependent manner, thereby presents an intracellular approach for controlled drug release.

3.4.2. Hyperspectral imaging

The hyperspectral imaging technique presents a reliable, high speed, and alternative to fluorescence imaging which can be used to differentiate various components within cells (Lu and

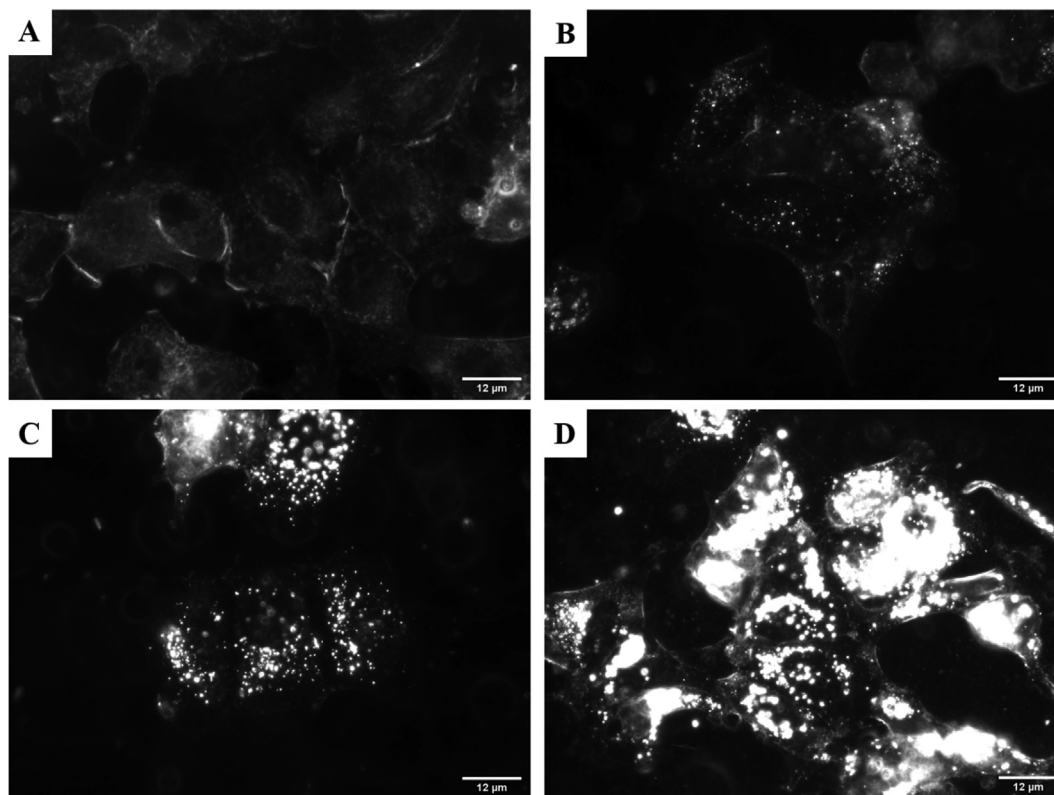


Fig. 5 Dark-field images of MCF-7 cells showing a time-dependent uptake of PS-modified Au@PdNDs.DOX. (A) Untreated control, (B) 2 h, (C) 6 h, (D) 24 h exposure time, respectively. Images were acquired at 60× magnification (Scale bar = 12 μm).

Fei, 2014; Mehta et al., 2018; Sohrabi Kashani et al., 2020). The morphology and composition of nanoparticles are two important factors that determine the characteristic spectral profiles of each compound (Mehta et al., 2021). The spectral signatures of nanocarriers loaded with fluorescent molecules like DOX can be assessed based on changes in the scattering properties before and after conjugation. Fig. 6A-B. shows the plasmonic-based reflectance spectra of bare PS. Au@PdNDs and PS.Au@PdNDs.DOX that enable the spectral differentiation of loaded and unloaded nanocarrier. Both PS.Au@PdNDs and PS.Au@PdNDs.DOX showed spectral variations in the profiles associated with each. To demonstrate the variations in the composition of the nanocarriers in the cell cytoplasm, we compared the mean reflectance spectral profiles from PS.Au@PdNDs and PS.Au@PdNDs.DOX in treated cells (Fig. 6C-D). The intense reflectance spectra (red lines) matched with those collected from PS.Au@PdNDs, PS. Au@PdNDs.DOX while the reflectance spectra from the cytoplasm (white line) and background (green line) were very broad (Yang et al., 2014). The unloaded PS.Au@PdNDs showed a peak around 630–640 nm which remained unchanged after DOX loading. The scattering spectra of PS. Au@PdNDs.DOX did not show any shift, indicating that DOX molecules were evenly attached to the surface of the PS.Au@PdNDs nanocarrier with no interparticle variation (Zamora-Perez et al., 2018). Moreso, the appearance of a nudge band around 450–480 nm was associated with DOX loading. This observation proved that the PS.Au@PdNDs. DOX nanocarriers were indeed internalized within the cells.

Consequently, hyperspectral imaging (HSI) and spectral angle mapping (SAM) integrated into CytoViva microscopy were used to further confirm the internalization and accumulation of the PS.Au@PdNDs.DOX with MCF-7 cells.

The combination of imaging and spectroscopy afforded by this technique can provide more data on the dynamics of cell-nanoparticle interactions and improve nanocarrier optimization for sufficient uptake. This technique scans and creates a spectral library from the known sample's reflectance spectra which are then used to distinguish between known (Fig. S3) and unknown spectra observed from the cell-nanoparticle interaction. Fig. 7A shows the hyperspectral image of MCF-7 cells treated with PS.Au@PdNDs.DOX. The appearance of bright spots within the cells was due to the high reflectance spectral property of the internalized nanocarrier. To ascertain whether PS.Au@PdNDs.DOX nanocarriers are present in the hyperspectral image, an automated procedure; spectral angle mapping (SAM) was used to identify the nanocarriers. As shown in Fig. 7B, the red dots observed in the SAM image indicated the locations of the PS-modified nanocarriers when compared with the reflectance spectral library of known PS. Au@PdNDs.DOX. The overlaid image in Fig. 7C showed the spectral angle mapped onto the hyperspectral image with the red dots representing the PS.Au@PdNDs.DOX.

3.4.3. Distribution of PS.Au@PdNDs.DOX within cells

We investigated the changes in the distribution of PS. Au@PdNDs.DOX internalized in cells using the 3D CytoViva fluorescence imaging technique. It is assumed that the PS-modified Au@PdNDs.DOX nanocarrier can travel through the cytoplasm via a receptor-mediated endocytotic pathway leading to its confinement in an endosome or lysosome. Fig. 8 illustrates the distribution of PS-conjugated Au@PdNDs.DOX within the cells. The images were acquired by rotating the cells across the Z-axis of a three-dimensional (3D) plane using the CytoViva software. The images clearly showed the localization of the nanocarriers within the cells.

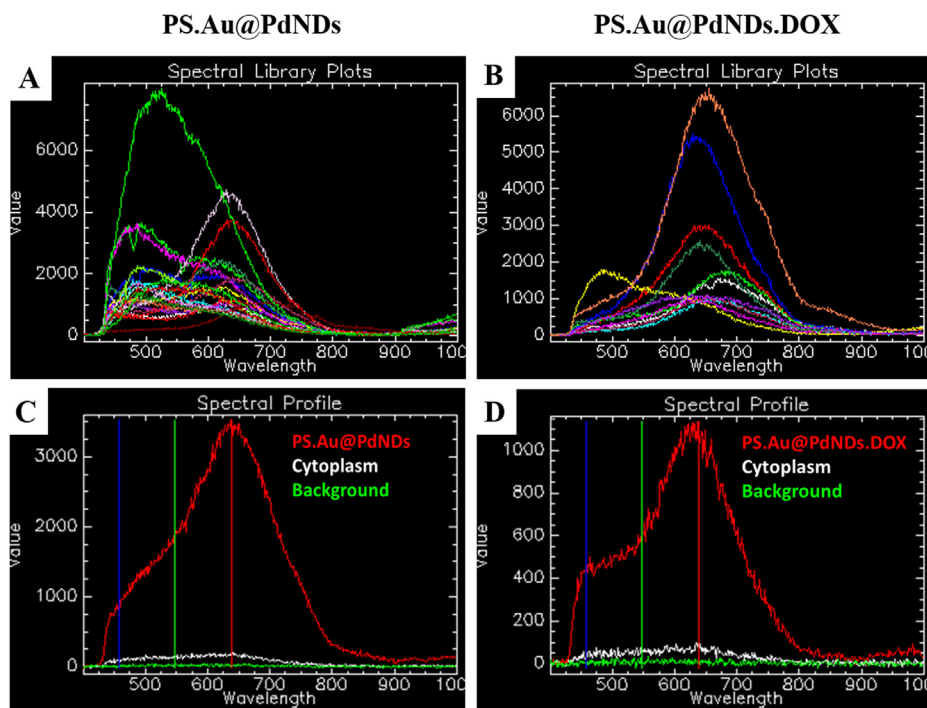


Fig. 6 Spectral profile of PS.Au@PdNDs.DOX internalized in MCF-7 cells at 2 h. Reflectance spectral libraries of (A) PS.Au@PdNDs (B) PS.Au@PdNDs.DOX and their respective mean spectral profiles after treatment in cells (C-D).

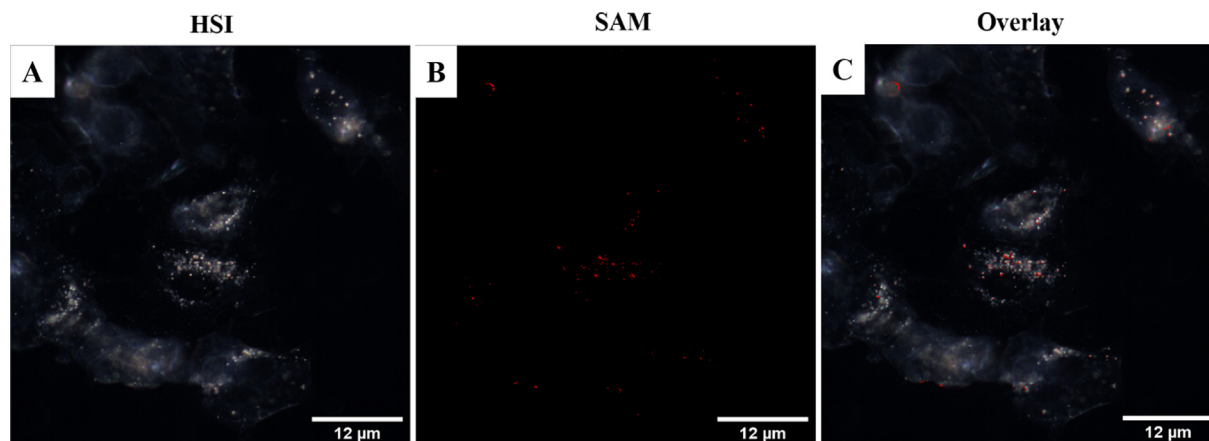


Fig. 7 Hyperspectral reflectance profile of PS.Au@PdNDs.DOX (red line), cytoplasm (white line), and background reflectance (green line) from the nucleus. Images were acquired at 60 \times magnification (Scale bar = 12 μ m).

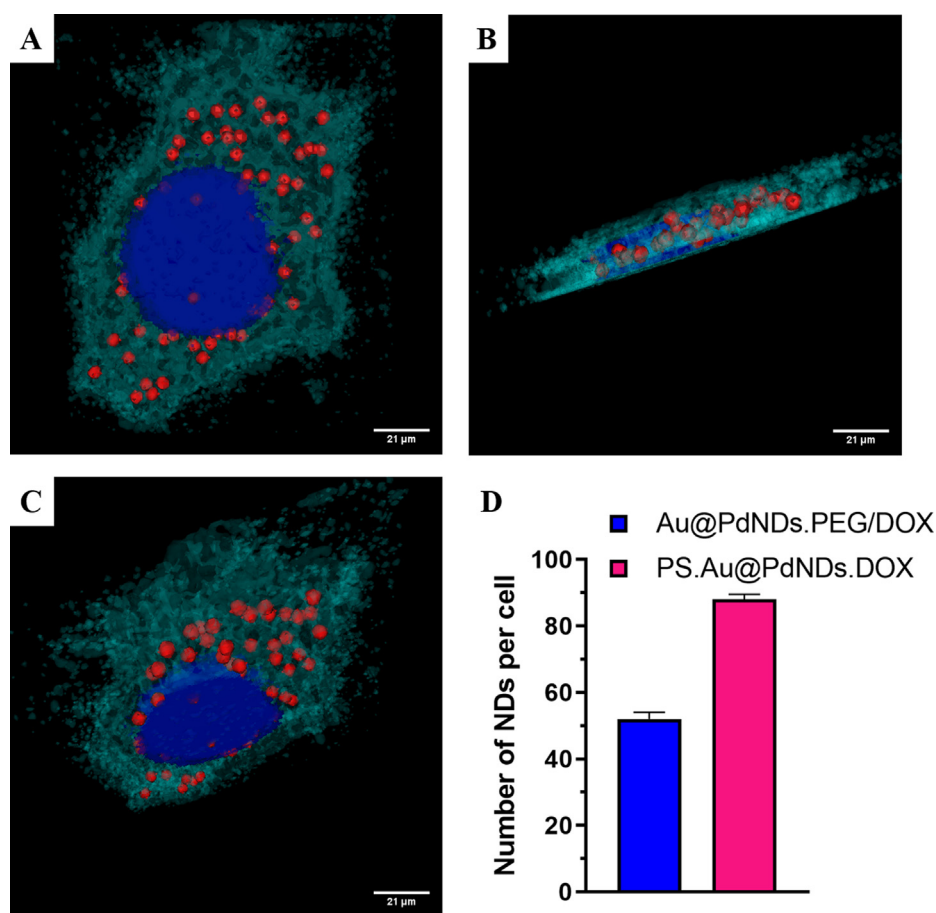


Fig. 8 3D-CytoViva fluorescent images of MCF-7 cells treated with PS.Au@PdNDs.DOX for 2 h. (A-C) The images were rotated along its focal plane in the direction of the Z-axis. Images were acquired at 60 \times magnification, scale bar = 21 μ m). (D) number of nanoparticles counted by CytoViva software within cells after 2 h incubation.

As shown in Fig. 8A-C, the red dots represent PS.Au@PdNDs.DOX and the cytoplasm in cyan color. The nanocarriers were distributed throughout the cytoplasm and could be seen migrating towards the nucleus. The nucleus (in blue color) showed the presence of the nanocarriers inside as

well at 2 h exposure. The endocytotic internalization of nanoparticles has been reported to occur via three main pathways: clathrin-mediated, caveolae-mediated, and macropinocytosis (Foroozandeh and Aziz, 2018; Yameen et al., 2014). As a passive targeting control, Au@PdNDs.

PEG/DOX nanocarriers based on enhanced permeability and retention (EPR) effect were treated against MCF-7 cells under a similar condition and compared (Fig. S4). The Au@PdNDs. PEG/DOX nanocarriers were also distributed within the cytoplasm. However, the Au@PdNDs. PEG/DOX nanocarriers were unable to cross beyond the nuclear membrane into the nuclear compartment as the nanocarrier assembled outside of the nuclear membrane. From the 3D-CytoViva analysis, an average of 87 and 52 nanoparticles were counted within the cells for PS.Au@PdNDs.DOX and Au@PdNDs. PEG/DOX respectively at 2 h incubation (Fig. 8D). These observations demonstrated that the PS.Au@PdNDs.DOX has a better intracellular accumulation potential with nuclear targeting capability than the Au@PdNDs. PEG/DOX nanocarrier. The dynamics of cell uptake from an active and passive targeting strategy have continued to generate research interests in the last decades (Attia et al., 2019). Interestingly, the receptor-mediated pathway has been proposed as a more efficient strategy to improve the accumulation of nanocarriers for drug delivery applications. A myriad of ligands such as transferrin (Zhao et al., 2018), folic acid (Xia et al., 2018), peptides (Yang et al., 2014), hyaluronic acid (Luo et al., 2020), aptamers (Li et al., 2019), etc. have been employed for the modification of nanocarriers to significantly enhance their targeting capabilities. A recent study demonstrated that PS@SiNP-pDNA gene nanocarriers were internalized via clathrin-mediated endocytosis (Ji et al., 2018). PS as a ligand can mediate the transport of Au@PdNDs resulting in enhanced uptake and rapid distribution as shown in our result. This novel visualization technique offers significant information regarding the distribution and the nuclear targeting capability of the PS-modified Au@PdNDs.DOX.

3.5. Therapeutic potentials of PS-modified Au@PdNDs.DOX

Previous studies have shown that DOX is effective against tumor cells and can destroy cancer cells via the induction of apoptosis (Xia et al., 2018). The release of phosphatidylserine (PS) from the inner layer of the cell membrane to the extracellular environment is a critical biomarker for apoptosis induction. Annexin V can bind to released PS, thereby enabling the precise measurement of apoptosis (Oladipo et al., 2020a). To analyze the mechanism of cell death and the changes that accompany the rate of induction of apoptosis, flow cytometry was used to evaluate whether PS.Au@PdNDs.DOX could exhibit greater induction of apoptosis in MCF-7 cells compared to free DOX or Au@PdNDs. PEG/DOX. Cells were treated with DOX, Au@PdNDs. PEG/DOX, and PS.Au@PdNDs.DOX at respective IC₅₀ values (µg/mL) for 24 h and 48 h after which apoptotic responses were assessed. As shown in Fig. 9, PS.Au@PdNDs.DOX treatment induced apoptosis in MCF-7 cells and resulted in a greater number of apoptotic cells (64.3%) at 24 h compared with cells exposed to DOX (40.1%) and Au@PdNDs. PEG/DOX (48.2%). When the treatment time was increased to 48 h, treatment with PS.Au@PdNDs.DOX led to a further increase in apoptosis rates (75.1%) with the DOX and passive targeted Au@PdNDs. PEG/DOX also showing increased apoptotic cell proportions at 54.4% and 70.2% respectively (Fig. S5). These results showed that PS.Au@PdNDs.DOX improved the anticancer efficiency of DOX when DOX is loaded onto the surface of

PS-modified Au@PdNDs nanocarrier. In rapidly proliferating breast adenocarcinoma cells like MCF-7, nucleolin; a nucleolar-binding phosphoprotein is abundantly overexpressed in the cell membrane and cytoplasm (Li et al., 2019; Watanabe et al., 2010). On the cancer cell surface, nucleolin provides a platform for protein attachment for several growth factors and ligands. The continuous intracellular migration of nucleolin into the nucleus thus confer nucleolin with active nuclear identification functionality (Dam et al., 2012; Qiu et al., 2015). It is anticipated that upon the treatment of cells with PS-modified Au@PdNDs.DOX, the PS-rich nuclear localization signal present on the surfaces of the PS.Au@PdNDs.DOX can bind onto nucleolin with high affinity and selectivity, thereby enabling its efficient transport to the nucleus. The recognition, specific binding, and accumulation of the arginine-rich cell-penetrating PS by nucleolin receptor on the surface of cancerous cells have been confirmed (Givens et al., 2018; Lafarga et al., 2018). Unlike cancer cells, nucleolin binding protein is generally not present outside the nucleus of normal cells, thus lacking the potential for intracellular transport. This perhaps could be the reason for the higher cell viability of PS.Au@PdNDs and PS.Au@PdNDs.DOX treatment against HEK 293 observed above. Hence, the observed apoptotic behavior of the PS.Au@PdNDs.DOX in MCF-7 cells was not surprising considering the enhanced accumulation and distribution within the cytoplasm as confirmed by darkfield microscopy, hyperspectral imaging, and 3D-CytoViva fluorescence imaging.

3.6. Cell cycle assay

A key factor in the control of tumor proliferation is the regulation of cell cycle progression (Murad et al., 2016). Cytotoxic compounds such as anticancer agents possess the ability to cause DNA damage by regulating the cell cycle at specific phases, thereby leading to the induction of apoptosis (Dziedzic et al., 2017). To further detect DNA fragmentation, the status of the cell cycle checkpoint induced by PS.Au@PdNDs.DOX inhibition on MCF-7 cells was assessed by flow cytometry. Fig. 10 shows the representative cell cycle with a typical pattern depicted as G1/G0, S, and G2/M phases after treatment with DOX, Au@PdNDs. PEG/DOX, and PS.Au@PdNDs.DOX in MCF-7. All treated cells showed a decrease in the G1/G0 phase (54.0% for DOX, 47.1% for Au@PdNDs. PEG/DOX, and 62.8% for PS.Au@PdNDs. DOX respectively) compared with 63.3% in the control. This treatment for 24 h resulted in a concomitant proportion of cells accumulating in the G2/M phase from the control group (17.0%) to (27.8%, 25.6%, and 18.9% for DOX, Au@PdNDs. PEG/DOX, and PS.Au@PdNDs.DOX respectively) (Fig. 10). Whereas, after 48 h treatment with PS.Au@PdNDs.DOX, the proportion of cells in the G2/M phase increased to 25.3% while that of the G0/G1 phase decreased to 57.0%. Also, treatment with Au@PdNDs. PEG/DOX showed an 18.3% decrease of the G2/M phase at 48 h compared to 25.6% at 24 h. These data suggested that PS.Au@PdNDs.DOX apoptotic induction was largely due to G2/M arrest. Consequently, the PS.Au@PdNDs.DOX treatment demonstrated a stronger capacity to induce higher cell death than Au@PdNDs. PEG/DOX. Hence, the differences in cell proportion exhibited by PS.Au@PdNDs.DOX in MCF-7 cells could partly be associated

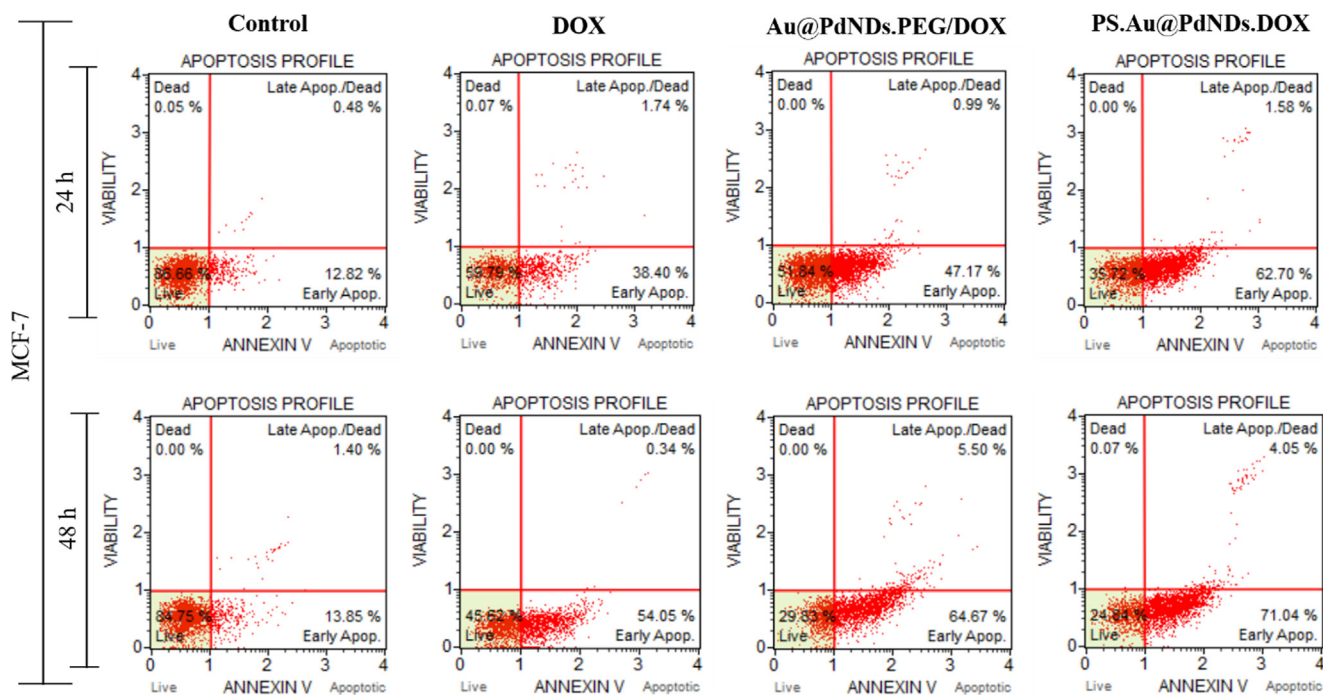


Fig. 9 Representative plots of apoptotic induction by Au@PdNds.PEG/DOX and PS.Au@PdNds.DOX on MCF-7 cells were treated for 24 h and 48 h at respective IC₅₀ values (μg/mL). The distribution of the rate of early and late apoptosis induced by PS.Au@PdNds.DOX was determined by flow cytometry and compared with negative control (untreated), positive control (DOX), and the passive targeted Au@PdNds.PEG/DOX.

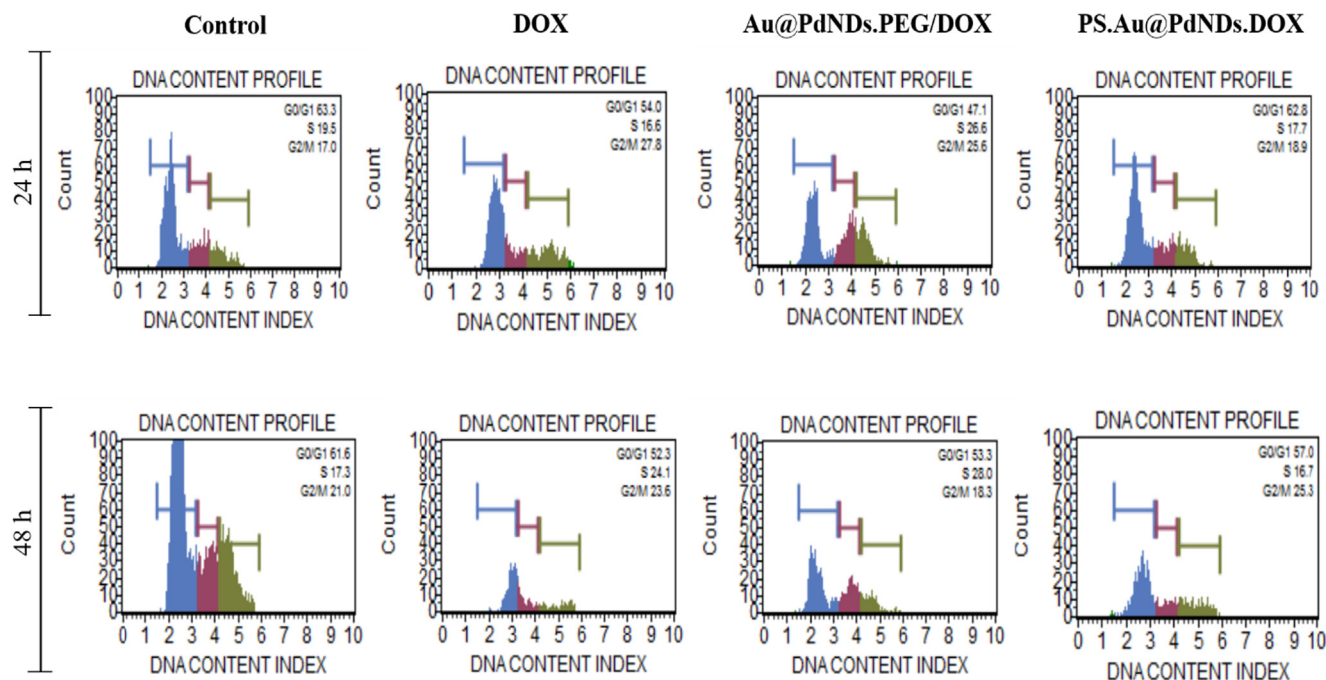


Fig. 10 Representative cell cycle distribution plots showing the cell cycle phase induction by DOX, Au@PdNds.PEG/DOX, and PS.Au@PdNds.DOX after treatment on MCF-7 cells for 24 h and 48 h. The untreated cells were used as the negative control.

with the improved intracellular localization of the PS-modified Au@PdNDs. However, we did not notice a significant difference in the cell cycle distribution among the different groups (Fig. S6). Several studies on the disruption of cell cycle progression have been reported for nanocarrier-based DOX delivery systems. Docetaxel (DTX) loaded folic acid-decorated PEG-PCL nanoparticles were found to retain the G2/M phase in tumor cells after cell internalization (Hu et al., 2016). The arrest of the G2/M cell cycle phase by DOX-tethered PVP-coated AuNPs was significantly enhanced in the treatment of lung cancer A549 cells (Ramalingam et al., 2018). Our results are in agreement with these studies and highlighted the relationship between cell cycle regulation and apoptosis induced by targeted nanocarrier-based drug delivery systems.

3.7. Mitochondrial membrane permeabilization

One of the main features of targeted delivery of anticancer drugs to tumor cells is the intrinsic apoptotic pathway via the induction of loss of mitochondrial membrane permeability (Liu et al., 2017). Since apoptosis can occur through several molecular pathways, the mitochondria pathway has been established as one which activates the release of apoptotic regulators usually found within the mitochondrial membrane pores (Shi et al., 2018). The mechanism of mitochondrial dysfunction results from the release of cytochrome *c*, a soluble protein from the mitochondrial membrane pores ruptured in response to drugs. The release of this protein into the cytosol is the hallmark of drug-triggered apoptotic events. To investigate whether mitochondrial membrane disruption mechanism contributed to the apoptotic events, mitochondrial membrane potential was measured using JC-10 fluores-

cence dye. From Fig. 11A, the treatment of MCF-7 cells against DOX, Au@PdNDs.PEG/DOX, and PS.Au@PdNDs.DOX at equivalent IC₅₀ values resulted in decreased fluorescence with a percentage decrease at 50.1%, 47.1%, and 61.2% respectively, when compared to the negative control. The PS.Au@PdNDs.DOX showed higher activity against MCF-7 cells compared to DOX and Au@PdNDs.PEG/DOX due to its significant inhibitory effect. These observations coincide with a decreased mitochondria membrane potential reported in HeLa cells upon triphenylphosphonium (TPP) conjugation to mesoporous silica nanoparticles (MSNPs) for the targeted delivery of DOX (Qu et al., 2015). These results possibly indicated that mitochondria-mediated pathways played a role in the induction of apoptosis in MCF-7 cells which may be attributed to the loss of their mitochondrial membrane potential.

3.8. Necrotic cell death

The loss of membrane integrity usually accompany cells undergoing necrosis and has been used to study necrotic cell death mechanism (Bhoola et al., 2020). When cytotoxic agents interfere with the normal functions of cells, it is commonly characterized by intracellular organelle rupture and swelling which triggers various inflammatory responses. This results in the intracellular release of lactate dehydrogenase (LDH) enzymes from the cytoplasm of damaged cells into the external surrounding thus providing a reliable biomarker for quantifying necrosis. To determine whether necrosis was a participating mechanism, MCF-7 cells were exposed to equivalent IC₅₀ values of DOX, Au@PdNDs.PEG/DOX, and PS.Au@PdNDs.DOX for 24 h and the released LDH was fluorometrically

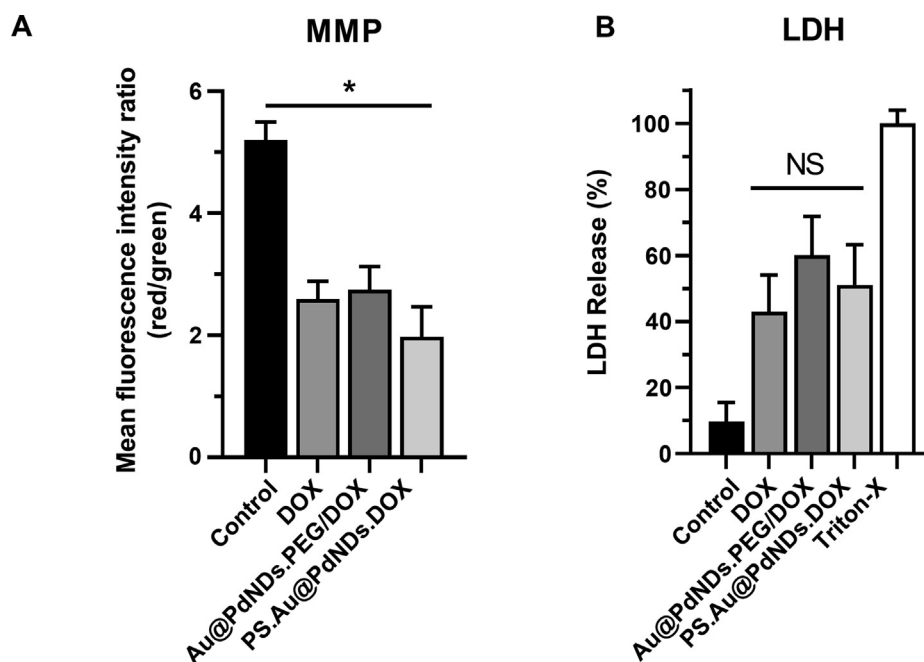


Fig. 11 (A) Mitochondrial membrane potential (MMP) detected (B) Assessment of necrosis by lactate dehydrogenase (LDH) release in MCF-7 cells upon treatment with DOX, Au@PdNDs.PEG/DOX, and PS.Au@PdNDs.DOX for 24 h (Triton-X solution induce maximum LDH release of 100%). Data were expressed as mean \pm SD (n = 3) with **P* < 0.05 considered statistically significant.

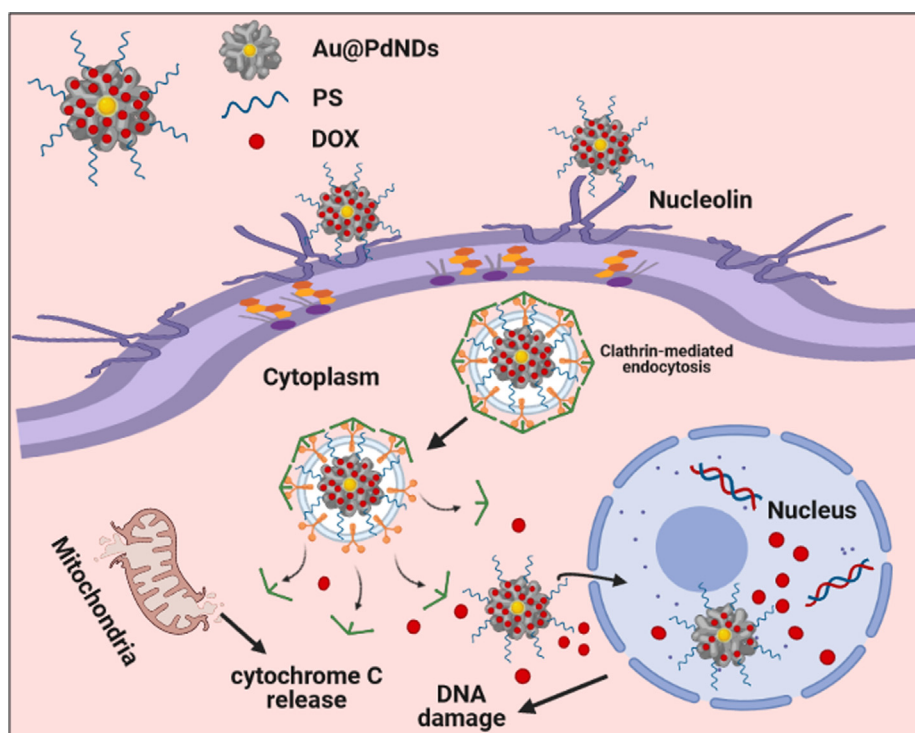


Fig. 12 Schematic illustration of the proposed anticancer mechanism of action of PS.Au@PdNDs.DOX nanocarrier in MCF-7 cells.

quantified. As shown in Fig. 11B, increased LDH release was observed for all treated groups. However, the changes in the leakage of cytosolic LDH enzyme detected among the different groups were not significant, thereby suggesting that minimal cell membrane damage occurred. This result indicated that apoptosis was the main mechanism of cell death which is consistent with the observed apoptotic induction by all groups as highlighted above. Consequently, we proposed a mechanism of action underlying the targeted PS.Au@PdNDs.DOX treatment on MCF-7 cells (Fig. 12).

4. Conclusions

A novel active-targeted protamine sulfate (PS)-modified, three-dimensional Au@PdNDs nanodendrites was successfully synthesized to deliver DOX to the nucleus of human breast carcinoma MCF-7 cells. It was found that the PS.Au@PdNDs nanocomplex demonstrated no apparent toxicity against MCF-7 cells while the PS.Au@PdNDs.DOX showed excellent time-dependent uptake in MCF-7 cells, resulting in improved cancer cells suppression compared with passive targeted Au@PdNDs.PEG/DOX and DOX alone. Furthermore, the 3D CytoViva fluorescence imaging technique revealed the significant accumulation and distribution of the PS-modified nanodendrites within the cytoplasm. The efficient localization of the PS.Au@PdNDs.DOX within the nucleus consequently led to enhanced antitumor DOX efficiency and induce cell apoptosis *in vitro*. Our results showed that the modification of Au@PdNDs with PS should provide a new strategy for the accumulation and sustained delivery of DOX in cancer theranostic applications.

Declaration of Competing Interest

The authors declare that they have no known competing financial interests or personal relationships that could have appeared to influence the work reported in this paper.

Acknowledgements

The authors would like to thank the University of South Africa through the Institute for Nanotechnology and Water Sustainability (iNanoWS), for financial assistance. Cell uptake experiments were carried out at the Biochemistry & Toxicology Section, National Institute for Occupational Health (NIOH), Johannesburg, South Africa. Fig. 12 was designed using <https://Biorender.com/>.

Appendix A. Supplementary material

Supplementary data to this article can be found online at <https://doi.org/10.1016/j.arabjc.2021.103344>.

References

- Attia, M.F., Anton, N., Wallyn, J., Omran, Z., Vandamme, T.F., 2019. An overview of active and passive targeting strategies to improve the nanocarriers efficiency to tumour sites. *J. Pharm. Pharmacol.* 71, 1185–1198. <https://doi.org/10.1111/jphp.13098>.
- Benyettou, F., Fahs, H., Elkharrag, R., Bilbeisi, R.A., Asma, B., Rezgui, R., Motte, L., Magzoub, M., Brandel, J., Olsen, J.C., Piano, F., Gunsalus, K.C., Platas-Iglesias, C., Trabolsi, A., 2017. Selective growth inhibition of cancer cells with doxorubicin-loaded CB[7]-modified iron-oxide nanoparticles. *RSC Adv.* 7, 23827–23834. <https://doi.org/10.1039/c7ra02693e>.

- Bhoora, S., Pather, Y., Marais, S., Punchoo, R., 2020. Cholecalciferol Inhibits Cell Growth and Induces Apoptosis in the CaSki Cell Line. *Med. Sci.* 8, 12. <https://doi.org/10.3390/medsci8010012>.
- Calamak, S., Ulubayram, K., 2019. Controlled synthesis of multi-branched gold nanodendrites by dynamic microfluidic flow system. *J. Mater. Sci.* 54, 7541–7552. <https://doi.org/10.1007/s10853-019-03403-0>.
- Cao, M., Deng, X., Su, S., Zhang, F., Xiao, X., Hu, Q., Fu, Y., Yang, B.B., Wu, Y., Sheng, W., Zeng, Y., 2013. Protamine sulfate-nanodiamond hybrid nanoparticles as a vector for MiR-203 restoration in esophageal carcinoma cells. *Nanoscale* 5, 12120–12125. <https://doi.org/10.1039/c3nr04056a>.
- Carvalho, C., Santos, R., Cardoso, S., Correia, S., Oliveira, P., Santos, M., Moreira, P., 2009. Doxorubicin: The Good, the Bad and the Ugly Effect. *Curr. Med. Chem.* 16, 3267–3285. <https://doi.org/10.2174/092986709788803312>.
- Cavalcante, C.H., Fernandes, R.S., de Oliveira Silva, J., Ramos Oda, C.M., Leite, E.A., Cassali, G.D., Charlie-Silva, I., Ventura Fernandes, B.H., Miranda Ferreira, L.A., de Barros, A.L.B., 2021. Doxorubicin-loaded pH-sensitive micelles: A promising alternative to enhance antitumor activity and reduce toxicity. *Biomed. Pharmacother.* 134, 111076. <https://doi.org/10.1016/j.biopha.2020.111076>.
- Dam, D.H.M., Lee, J.H., Sisco, P.N., Co, D.T., Zhang, M., Wasielewski, M.R., Odom, T.W., 2012. Direct observation of nanoparticle-cancer cell nucleus interactions. *ACS Nano* 6, 3318–3326. <https://doi.org/10.1021/nn300296p>.
- Du, Y., Xia, L., Jo, A., Davis, R.M., Bissel, P., Ehrich, M.F., Kingston, D.G.I., 2018. Synthesis and Evaluation of Doxorubicin-Loaded Gold Nanoparticles for Tumor-Targeted Drug Delivery. *Bioconjug. Chem.* 29. <https://doi.org/10.1021/acs.bioconjchem.7b00756>.
- Dziedzic, A., Kubina, R., Kabała-Dzik, A., Tanasiewicz, M., 2017. Induction of Cell Cycle Arrest and Apoptotic Response of Head and Neck Squamous Carcinoma Cells (Detroit 562) by Caffeic Acid and Caffeic Acid Phenethyl Ester Derivative. Evidence-based Complement. *Altern. Med.* 2017, 1–10. <https://doi.org/10.1155/2017/6793456>.
- Foroozandeh, P., Aziz, A.A., 2018. Insight into Cellular Uptake and Intracellular Trafficking of Nanoparticles. *Nanoscale Res. Lett.* 13, 1–12. <https://doi.org/10.1186/s11671-018-2728-6>.
- Givens, B.E., Naguib, Y.W., Geary, S.M., Devor, E.J., Salem, A.K., 2018. Nanoparticle-Based Delivery of CRISPR/Cas9 Genome-Editing Therapeutics. *AAPS J.* 20, 1–22. <https://doi.org/10.1208/s12248-018-0267-9>.
- Halim, V.A., García-Santisteban, I., Warmerdam, D.O., Van Den Broek, B., Heck, A.J.R., Mohammed, S., Medema, R.H., 2018. Doxorubicin-induced DNA damage causes extensive ubiquitination of ribosomal proteins associated with a decrease in protein translation. *Mol. Cell. Proteomics* 17, 2297–2308. <https://doi.org/10.1074/mcp.RA118.000652>.
- Hiebl, B., Peters, S., Gemeinhardt, O., Niehues, S.M., Jung, F., 2017. Impact of serum in cell culture media on in vitro lactate dehydrogenase (LDH) release determination. *J. Cell. Biotechnol.* 3, 9–13. <https://doi.org/10.3233/jcb-179002>.
- Hu, G., Cun, X., Ruan, S., Shi, K., Wang, Y., Kuang, Q., Hu, C., Xiao, W., He, Q., Gao, H., 2016. Utilizing G2/M retention effect to enhance tumor accumulation of active targeting nanoparticles. *Sci. Rep.* 6, 1–10. <https://doi.org/10.1038/srep27669>.
- Jang, H., Ryoo, S.R., Kostarelos, K., Han, S.W., Min, D.H., 2013. The effective nuclear delivery of doxorubicin from dextran-coated gold nanoparticles larger than nuclear pores. *Biomaterials* 34, 3503–3510. <https://doi.org/10.1016/j.biomaterials.2013.01.076>.
- Ji, X., Wang, C., Tang, M., Guo, D., Peng, F., Zhong, Y., Song, B., Su, Y., He, Y., 2018. Biocompatible protamine sulfate@silicon nanoparticle-based gene nanocarriers featuring strong and stable fluorescence. *Nanoscale* 10, 14455–14463. <https://doi.org/10.1039/c8nr03107j>.
- Jia, D., Ma, X., Lu, Y., Li, X., Hou, S., Gao, Y., Xue, P., Kang, Y., Xu, Z., 2021. ROS-responsive cyclodextrin nanoplatform for combined photodynamic therapy and chemotherapy of cancer. *Chinese Chem. Lett.* 32, 162–167. <https://doi.org/10.1016/j.ccllet.2020.11.052>.
- Kumari, S., Ram, B., Kumar, D., Ranote, S., Chauhan, G.S., 2018. Nanoparticles of oxidized-cellulose synthesized by green method. *Mater. Sci. Energy Technol.* 1, 22–28. <https://doi.org/10.1016/j.mset.2018.04.003>.
- Lafarga, V., Sirozh, O., Hisaoka, M., Zarzuela, E., Boskovic, J., Jovanovic, B., 2018. DNA and RNA binding mediate the toxicity of arginine-rich peptides encoded by C9ORF72 GGGGCC repeats. *BioRxiv*, 1–21.
- Li, X., Wu, X., Yang, H., Li, L., Ye, Z., Rao, Y., 2019. A nuclear targeted Dox-aptamer loaded liposome delivery platform for the circumvention of drug resistance in breast cancer. *Biomed. Pharmacother.* 117, 109072. <https://doi.org/10.1016/j.biopha.2019.109072>.
- Liu, X., Zhang, X., Zhu, M., Lin, G., Liu, J., Zhou, Z., Tian, X., Pan, Y., 2017a. PEGylated Au@Pt Nanodendrites as Novel Theranostic Agents for Computed Tomography Imaging and Photothermal/Radiation Synergistic Therapy. *ACS Appl. Mater. Interfaces* 9, 279–285. <https://doi.org/10.1021/acsami.6b15183>.
- Liu, Y., Zhang, X., Zhou, M., Nan, X., Chen, X., Zhang, X., 2017b. Mitochondrial-Targeting Nonamine-Doxorubicin Nanoparticles for Synergistic Chemotherapy to Conquer Drug Resistance. *ACS Appl. Mater. Interfaces* 9, 43498–43507. <https://doi.org/10.1021/acsami.7b14577>.
- Lu, G., Fei, B., 2014. Medical hyperspectral imaging: a review. *J. Biomed. Opt.* 19, 010901. <https://doi.org/10.1117/1.jbo.19.1.010901>.
- Luo, S., Feng, J., Xiao, L., Guo, L., Deng, L., Du, Z., Xue, Y., Song, X., Sun, X., Zhang, Z., Fu, Y., Gong, T., 2020. Targeting self-assembly peptide for inhibiting breast tumor progression and metastasis. *Biomaterials* 249, 120055. <https://doi.org/10.1016/j.biomaterials.2020.120055>.
- Maney, V., Singh, M., 2019. The synergism of platinum-gold bimetallic nanoconjugates enhances 5-fluorouracil delivery in vitro. *Pharmaceutics* 11, 439. <https://doi.org/10.3390/pharmaceutics11090439>.
- Maney, V., Singh, M., 2017. An in vitro assessment of novel chitosan/bimetallic PtAu nanocomposites as delivery vehicles for doxorubicin. *Nanomedicine* 12, 1–16. <https://doi.org/10.2217/nnm-2017-0228>.
- Marinello, J., Delcuratolo, M., Capranico, G., 2018. Anthracyclines as Topoisomerase II poisons: From early studies to new perspectives. *Int. J. Mol. Sci.* 19, 1–18. <https://doi.org/10.3390/ijms19113480>.
- Mehta, N., Sahu, S.P., Shaik, S., Devireddy, R., Gartia, M.R., 2021. Dark-field hyperspectral imaging for label free detection of nanobio-materials. *Wiley Interdiscip. Rev. Nanomedicine Nanobiotechnology* 13, 1–28. <https://doi.org/10.1002/wnan.1661>.
- Mehta, N., Shaik, S., Devireddy, R., Gartia, M.R., 2018. Single-Cell Analysis Using Hyperspectral Imaging Modalities. *J. Biomech. Eng.* 140, 020802–20816. <https://doi.org/10.1115/1.4038638>.
- Mizutani, H., Tada-Oikawa, S., Hiraku, Y., Kojima, M., Kawanishi, S., 2005. Mechanism of apoptosis induced by doxorubicin through the generation of hydrogen peroxide. *Life Sci.* 76, 1439–1453. <https://doi.org/10.1016/j.lfs.2004.05.040>.
- Murad, H., Hawat, M., Ekhtiar, A., AlJapawe, A., Abbas, A., Darwish, H., Sbenati, O., Ghannam, A., 2016. Induction of G1-phase cell cycle arrest and apoptosis pathway in MDA-MB-231 human breast cancer cells by sulfated polysaccharide extracted from *Laurencia papillosa*. *Cancer Cell Int.* 16, 1–11. <https://doi.org/10.1186/s12935-016-0315-4>.
- Nair, P.R., 2019. Delivering combination chemotherapies and targeting oncogenic pathways via polymeric drug delivery systems. *Polymers (Basel)* 11, 1–34. <https://doi.org/10.3390/polym11040630>.

- Oladipo, A.O., Iku, S.I.I., Ntwasa, M., Nkambule, T.T.I., Mamba, B. B., Msagati, T.A.M., 2020a. Doxorubicin conjugated hydrophilic AuPt bimetallic nanoparticles fabricated from *Phragmites australis*: Characterization and cytotoxic activity against human cancer cells. *J. Drug Deliv. Sci. Technol.* 57. <https://doi.org/10.1016/j.jddst.2020.101749>.
- Oladipo, A.O., Nkambule, T.T.I., Mamba, B.B., Msagati, T.A.M., 2020b. Therapeutic nanodendrites: Current applications and prospects. *Nanoscale Adv.* 2, 5152–5165. <https://doi.org/10.1039/d0na00672f>.
- Oladipo, A.O., Nkambule, T.T.I., Mamba, B.B., Msagati, T.A.M., 2020c. The stimuli-responsive properties of doxorubicin adsorbed onto bimetallic Au @ Pd nanodendrites and its potential application as drug delivery platform. *Mater. Sci. Eng. C* 110, 110696. <https://doi.org/10.1016/j.msec.2020.110696>.
- Oladipo, A.O., Oluwafemi, O.S., Songca, S.P., Sukhbaatar, A., Mori, S., Okajima, J., Komiya, A., Maruyama, S., Kodama, T., 2017. A novel treatment for metastatic lymph nodes using lymphatic delivery and photothermal therapy. *Sci. Rep.* 7, 45459. <https://doi.org/10.1038/srep45459>.
- Oladipo, A.O., Unuofin, J.O., Iku, S.I.I., Nkambule, T.T.I., Mamba, B.B., Msagati, T.A.M., 2021. Bimetallic Au @ Pd nanodendrite system incorporating multimodal intracellular imaging for improved doxorubicin antitumor efficiency. *Int. J. Pharm.* 602, 120661. <https://doi.org/10.1016/j.ijpharm.2021.120661>.
- Phan, T.T.V., Huynh, T.C., Manivasagan, P., Mondal, S., Oh, J., 2020. An up-to-date review on biomedical applications of palladium nanoparticles. *Nanomaterials* 10, 1–19. <https://doi.org/10.3390/nano10010066>.
- Pilco-Ferreto, N., Calaf, G.M., 2016. Influence of doxorubicin on apoptosis and oxidative stress in breast cancer cell lines. *Int. J. Oncol.* 49, 753–762. <https://doi.org/10.3892/ijo.2016.3558>.
- Puras, G., Martínez-Navarrete, G., Mashal, M., Zárate, J., Agirre, M., Ojeda, E., Grijalvo, S., Eritja, R., Diaz-Tahoces, A., Avilés-Trigueros, M., Fernández, E., Pedraz, J.L., 2015. Protamine/DNA/niosome ternary nonviral vectors for gene delivery to the retina: The role of protamine. *Mol. Pharm.* 12, 3658–3671. <https://doi.org/10.1021/acs.molpharmaceut.5b00422>.
- Qiu, L., Chen, T., Öçsoy, I., Yasun, E., Wu, C., Zhu, G., You, M., Han, D., Jiang, J., Yu, R., Tan, W., 2015. A cell-targeted, size-photocontrollable, nuclear-uptake nanodrug delivery system for drug-resistant cancer therapy. *Nano Lett.* 15, 457–463. <https://doi.org/10.1021/nl503777s>.
- Qiu, P., Yang, M., Qu, X., Huai, Y., Zhu, Y., Mao, C., 2016. Tuning photothermal properties of gold nanodendrites for in vivo cancer therapy within a wide near infrared range by simply controlling their degree of branching. *Biomaterials* 104, 138–144. <https://doi.org/10.1016/j.biomaterials.2016.06.033>.
- Qu, Q., Ma, X., Zhao, Y., 2015. Targeted delivery of doxorubicin to mitochondria using mesoporous silica nanoparticle nanocarriers. *Nanoscale* 7, 16677–16686. <https://doi.org/10.1039/c5nr05139h>.
- Ramalingam, V., Varunkumar, K., Ravikumar, V., Rajaram, R., 2018. Target delivery of doxorubicin tethered with PVP stabilized gold nanoparticles for effective treatment of lung cancer. *Sci. Rep.* 8, 1–12. <https://doi.org/10.1038/s41598-018-22172-5>.
- Rayner, D.M., Cutts, S.M., 2014. Anthracyclines, in: *Side Effects of Drugs Annual*. <https://doi.org/10.1016/B978-0-444-63407-8.00045-9>.
- Shi, M., Zhang, J., Li, X., Pan, S., Li, J., Yang, C., Hu, H., Qiao, M., Chen, D., Zhao, X., 2018. Mitochondria-targeted delivery of doxorubicin to enhance antitumor activity with HER-2 peptide-mediated multifunctional pH-sensitive DQAsomes. *Int. J. Nanomedicine* 13, 4209–4226. <https://doi.org/10.2147/IJN.S163858>.
- Sinha, B.K., 2020. Role of Oxygen and Nitrogen Radicals in the Mechanism of Anticancer Drug Cytotoxicity. *J. Cancer Sci. Ther.* 12, 10–18.
- Sohrabi Kashani, A., Piekny, A., Packirisamy, M., 2020. Using intracellular plasmonics to characterize nanomorphology in human cells. *Microsystems Nanoeng.* 6, 1–14. <https://doi.org/10.1038/s41378-020-00219-w>.
- Suarasan, S., Focsan, M., Potara, M., Soritau, O., Florea, A., Maniu, D., Astilean, S., 2016. Doxorubicin-incorporated nanotherapeutic delivery system based on gelatin-coated gold nanoparticles: Formulation, drug release, and multimodal imaging of cellular internalization. *ACS Appl. Mater. Interfaces* 8, 22900–22913. <https://doi.org/10.1021/acsami.6b07583>.
- Ünlü, A., Meran, M., Dinc, B., Karatepe, N., Bektaş, M., Güner, F.S., 2018. Cytotoxicity of doxorubicin loaded single-walled carbon nanotubes. *Mol. Biol. Rep.* 45, 523–531. <https://doi.org/10.1007/s11033-018-4189-5>.
- Wang, C., Qi, P., Lu, Y., Liu, L., Zhang, Y., Sheng, Q., Wang, T., Zhang, M., Wang, R., Song, S., 2020. Bicomponent polymeric micelles for pH-controlled delivery of doxorubicin. *Drug Deliv.* 27, 344–357. <https://doi.org/10.1080/10717544.2020.1726526>.
- Watanabe, T., Hirano, K., Takahashi, A., Yamaguchi, K., Beppu, M., Fujiki, H., Suganuma, M., 2010. Nucleolin on the cell surface as a new molecular target for gastric cancer treatment. *Biol. Pharm. Bull.* 33, 796–803. <https://doi.org/10.1248/bpb.33.796>.
- Wu, R., Liu, J., Chen, D., Pan, J., 2019. Carbon Nanodots Modified with Catechol-Borane Moieties for pH-Stimulated Doxorubicin Delivery: Toward Nuclear Targeting. *ACS Appl. Nano Mater.* 2, 4333–4341. <https://doi.org/10.1021/acsnm.9b00779>.
- Xia, Y., Xu, T., Zhao, M., Hua, L., Chen, Y., Wang, C., Tang, Y., Zhu, B., 2018. Delivery of Doxorubicin for Human Cervical Carcinoma Targeting Therapy by Folic Acid-Modified Selenium Nanoparticles. *Int. J. Mol. Sci.* 19, 1–14. <https://doi.org/10.3390/ijms19113582>.
- Xie, M., Zhang, F., Liu, L., Zhang, Y., Li, Y., Li, H., Xie, J., 2018. Surface modification of graphene oxide nanosheets by protamine sulfate/sodium alginate for anti-cancer drug delivery application. *Appl. Surf. Sci.* 440, 853–860. <https://doi.org/10.1016/j.apsusc.2018.01.175>.
- Yameen, B., Choi, W.I., Vilos, C., Swami, A., Shi, J., Farokhzad, O. C., 2014. Insight into nanoparticle cellular uptake and intracellular targeting. *J. Control. Release* 190, 485–499. <https://doi.org/10.1016/j.jconrel.2014.06.038>.
- Yang, C., Uertz, J., Yohan, D., Chithrani, B.D., 2014. Peptide modified gold nanoparticles for improved cellular uptake, nuclear transport, and intracellular retention. *Nanoscale* 6, 12026–12033. <https://doi.org/10.1039/c4nr02535k>.
- Yang, L., Wang, Z., Wang, J., Jiang, W., Jiang, X., Bai, Z., He, Y., Jiang, J., Wang, D., Yang, Li, 2016. Doxorubicin conjugated functionalizable carbon dots for nucleus targeted delivery and enhanced therapeutic efficacy. *Nanoscale* 8, 6801–6809. <https://doi.org/10.1039/c6nr00247a>.
- Yang, Q., Peng, J., Xiao, Y., Li, W., Tan, L., Xu, X., Qian, Z., 2018. Porous Au@Pt Nanoparticles: Therapeutic Platform for Tumor Chemo-Photothermal Co-Therapy and Alleviating Doxorubicin-Induced Oxidative Damage. *ACS Appl. Mater. Interfaces* 10, 150–164. <https://doi.org/10.1021/acsami.7b14705>.
- Yu, W., Zhan, Y., Xue, B., Dong, Y., Wang, Y., Jiang, P., Wang, A., Sun, Y., Yang, Y., 2018. Highly efficient cellular uptake of a cell-penetrating peptide (CPP) derived from the capsid protein of porcine circovirus type 2. *J. Biol. Chem.* 293, 15221–15232. <https://doi.org/10.1074/jbc.RA118.004823>.
- Yuan, Y., Guo, B., Hao, L., Liu, N., Lin, Y., Guo, W., Li, X., Gu, B., 2017. Doxorubicin-loaded environmentally friendly carbon dots as a novel drug delivery system for nucleus targeted cancer therapy. *Colloids Surfaces B Biointerfaces* 159, 349–359. <https://doi.org/10.1016/j.colsurfb.2017.07.030>.

- Zamora-Perez, P., Tsoutsis, D., Xu, R., Rivera-Gil, P., 2018. Hyperspectral-enhanced dark field microscopy for single and collective nanoparticle characterization in biological environments. *Materials (Basel)*. 11, 1–13. <https://doi.org/10.3390/ma11020243>.
- Zhao, S., Zhu, X., Cao, C., Sun, J., Liu, J., 2018. Transferrin modified ruthenium nanoparticles with good biocompatibility for photothermal tumor therapy. *J. Colloid Interface Sci.* 511, 325–334. <https://doi.org/10.1016/j.jcis.2017.10.023>.
- Zhong, J., Li, L., Zhu, X., Guan, S., Yang, Q., Zhou, Z., Zhang, Z., Huang, Y., 2015. A smart polymeric platform for multistage nucleus-targeted anticancer drug delivery. *Biomaterials* 65, 43–55. <https://doi.org/10.1016/j.biomaterials.2015.06.042>.
- Zhou, Y., Wang, D., Li, Y., 2014. Pd and Au@Pd nanodendrites: a one-pot synthesis and their superior catalytic properties. *Chem. Commun. (Camb)* 50, 6141–6144. <https://doi.org/10.1039/c4cc02081b>.